

Turbulent Aeroheating Testing of Mars Science Laboratory Entry Vehicle

Brian R. Hollis^{*}

NASA Langley Research Center, Hampton, VA, 23681

Arnold S. Collier[†]

AEDC White Oak, Silver Spring, MD 20901

An experimental investigation of turbulent aeroheating on the Mars Science Laboratory entry vehicle heat shield has been conducted in the Arnold Engineering Development Center Hypervelocity Wind Tunnel No. 9. Testing was performed on a 6-in. (0.1524 m) diameter MSL model in pure N₂ gas in the tunnel's Mach 8 and Mach 10 nozzles at free stream Reynolds numbers of $4.1 \times 10^6/\text{ft}$ to $49 \times 10^6/\text{ft}$ ($1.3 \times 10^7/\text{m}$ to $16 \times 10^7/\text{m}$) and $1.2 \times 10^6/\text{ft}$ to $19 \times 10^6/\text{ft}$ ($0.39 \times 10^7/\text{m}$ to $62 \times 10^7/\text{m}$), respectively. These conditions were sufficient to span the regime of boundary-layer flow from completely laminar to fully-developed turbulent flow over the entire forebody. A supporting aeroheating test was also conducted in the Langley Research Center 20-Inch Mach 6 Air Tunnel at free stream Reynolds number of $1 \times 10^6/\text{ft}$ to $7 \times 10^6/\text{ft}$ ($0.36 \times 10^7/\text{m}$ to $2.2 \times 10^7/\text{m}$) in order to help corroborate the Tunnel 9 results. A complementary computational fluid dynamics study was conducted in parallel to the wind tunnel testing. Laminar and turbulent predictions were generated for the wind tunnel test conditions and comparisons were performed with the data for the purpose of helping to define uncertainty margins on predictions for aeroheating environments during entry into the Martian atmosphere. Data from both wind tunnel tests and comparisons with the predictions are presented herein. It was concluded from these comparisons that for

^{*} Aerospace Engineer, Aerothermodynamics Branch, AIAA Senior Member

[†] Project Engineer

perfect-gas conditions, the computational tools could predict fully-laminar or fully-turbulent heating conditions to within $\pm 12\%$ or better of the experimental data.

Nomenclature

c_p	=	specific heat of test gas
$(c_p)_m$	=	specific heat of model material
D	=	maximum vehicle diameter
$(k)_m$	=	thermal conductivity of model material
ΔH	=	total enthalpy relative to wall conditions
L/D	=	aerodynamic lift-to-drag ratio
M_∞	=	free stream Mach number
M_e	=	boundary-layer edge Mach number
p_∞	=	free stream pressure
q	=	heat transfer rate
R_{base}	=	base (maximum) radius
R_{corner}	=	corner radius
R_{nose}	=	nose radius
Re_∞	=	free stream unit Reynolds Number
$Re_{\infty,D}$	=	free stream Reynolds Number based on diameter
Re_θ	=	boundary-layer momentum thickness Reynolds Number
St	=	Stanton number
T_∞	=	free stream temperature
U_∞	=	free stream velocity
x/R	=	normalized distance along model centerline
α	=	angle of attack
θ	=	boundary-layer momentum thickness
θ_F	=	forebody cone half-angle
θ_{aft1}	=	1st aftbody cone half-angle

θ_{aft2}	=	2nd aftbody cone half-angle
$(\rho)_m$	=	density of model material
ρ_∞	=	free stream density
μ_∞	=	free stream viscosity

I. □ Background

The Mars Science Laboratory (MSL) mission^{1,2}, which is scheduled to be launched in 2009, will perform the first precision landing of a large (>3000 kg) scientific payload on the surface of Mars in 2010. While the basic vehicle configuration, a 70-deg sphere-cone forebody with a conic or biconic aftbody, will be similar to those of previous Mars missions such as Viking, Pathfinder or Mars Exploration Rover (MER), the MSL design is both larger and heavier than previous designs (Table 1). To accomplish a precision landing, the vehicle will be required to fly a controlled lifting trajectory; current designs call for a lift-to-drag ratio (L/D) of 0.24, which will be generated by flying at an angle-of-attack of -16 deg. As a result of its high ballistic coefficient, MSL will experience heating levels higher than any of the previous missions, and furthermore, because of the high angle-of-attack (for a blunt body) flight requirement, the flow over the leeside of the forebody is expected to become turbulent early in the trajectory, which will substantially augment both the heating rates and loads above the laminar levels³.

Because there are relatively little data on the turbulent heating of very large-angle blunt cones such as the MSL entry vehicle, an extensive test program has been conducted to obtain data with which the accuracy of Computational Fluid Dynamics (CFD) tools used to predict flight environments can be compared. To-date, tests have been performed⁴⁻⁷ in the NASA Langley Research Center 20-Inch Mach 6 Air Tunnel (heat-shield penetration effects, perfect-gas environments, transition onset), the Calspan University of Buffalo (CUBRC) Large-Energy National Shock (LENS) Tunnel (low-to-moderate enthalpy reacting CO₂ environments, transition onset and turbulent heating), and the Graduate Aeronautical Laboratories of the California Institute of Technology (GALCIT) T5 Hypervelocity Shock Tunnel (moderate to high-enthalpy reacting CO₂ environments, and turbulent heating).

The test detailed herein was performed in perfect-gas N₂ in the Arnold Engineering Development Center (AEDC) Tunnel 9. Data were obtained across a very wide range of Reynolds numbers in order to evaluate the accuracy of CFD tools at predicting turbulent flows in an environment free from the chemical non-equilibrium effects present in the CUBRC LENS and GALCIT T5 tests. In addition to the AEDC Tunnel 9 test, a small amount

of data was also obtained in the LaRC 20-Inch Mach 6 Air Tunnel using the same wind tunnel model for comparison to the AEDC results. These two tests are expected to complete the heat-shield aeroheating test program.

II. □ Experimental Method

A. Facility Descriptions

1. *AEDC Tunnel 9 Description*

The Air Force's Arnold Engineering Development Center Tunnel 9, located in Silver Spring, Maryland, is a hypersonic, nitrogen-gas, blow-down wind tunnel with interchangeable nozzles that allow for testing at Mach numbers of 7, 8, 10, and 14 over a $0.054 \times 10^6/\text{ft}$ to $48.4 \times 10^6/\text{ft}$ ($0.177 \times 10^6/\text{m}$ to $158.8 \times 10^6/\text{m}$) unit Reynolds number range. A schematic drawing of the facility is shown in Figure 1 and a full description of the facility can be found in Ref. 8. The test section is a 5 ft (1.52 m) diameter, 12 ft (3.66 m) long cell that enables testing of large-scale model configurations. Tunnel 9 features a pitch system that can sweep models from -10 deg to 50 deg at pitch rates up to 80 deg/sec. With the tunnel's 0.2 sec to 15 sec run times, the dynamic pitch capability allows for a large volume of data to be captured over an entire range of pitch angles during a single run.

2. *LaRC 20-Inch Mach 6 Air Tunnel Description*

The NASA Langley Research Center 20-Inch Mach 6 Air Tunnel is a blow-down facility in which heated, dried, and filtered air is used as the test gas. The tunnel has a two dimensional, contoured nozzle that opens into a 0.521 m x 0.508 m (20.5 in. x 20.0 in.) test section. The tunnel is equipped with a bottom-mounted injection system that can transfer a model from the sheltered model box to the tunnel centerline in less than 0.5 sec. Run times of up to 15 minutes are possible in this facility, although for the current aeroheating study, run times of only a few seconds were required. The nominal reservoir conditions of this facility are stagnation pressures of 206.8 to 3447.4 kPa (30 to 500 psia) with stagnation temperatures of 422.2 to 555.5 K (760 °R to 1000 °R), which produce perfect-gas free stream flows with Mach numbers between 5.8 and 6.1 and Reynolds numbers of $1.64 \times 10^6/\text{m}$ to $23.3 \times 10^6/\text{m}$ ($0.5 \times 10^6/\text{ft}$ to $7.3 \times 10^6/\text{ft}$). A more detailed description of this facility is presented in Ref. 9.

B. Test Parametrics

1. AEDC Tunnel 9 Test Parametrics

The primary focus of this study was a 22 run test performed in Tunnel 9, with 7 runs in the tunnel's Mach 10 nozzle and 15 runs in the Mach 8 nozzle. The run matrix for this test is presented in Table 2. The Mach 10 runs (3020 to 3026) spanned a free stream Reynolds number range of $1.2 \times 10^6/\text{ft}$ to $19.1 \times 10^6/\text{ft}$ and the Mach 8 runs spanned a range of $4.1 \times 10^6/\text{ft}$ to $45 \times 10^6/\text{ft}$. All Mach 10 runs were performed in continuous pitch-sweep data acquisition mode over a nominal range of 0 deg to 26 deg, although the span shrank somewhat at the higher Reynolds numbers due to shorter run times. The initial Mach 8 runs (3027 to 3030) also were performed with a continuous pitch sweep over the same range, but it was found that the duration of good flow was shorter than expected and data at the beginning and end of the runs showed signs of transient behavior. Several Mach 8 runs (3042 to 3049) were then performed at fixed angle of attack (0 deg or 16 deg) in order to define the period of acceptable flow quality at each condition. Additional runs (3050 to 3053) with shorter pitch-sweeps centered in the high-quality flow period were then performed to span the range of ~ 8 deg to 22 deg angle of attack required by the MSL program.

In general, the Mach 10 conditions produced laminar flow except at the $14.6 \times 10^6/\text{ft}$ condition where leeside transition was clearly evident and at the $18.5 \times 10^6/\text{ft}$ and $19.1 \times 10^6/\text{ft}$ conditions where turbulent leeside flow was produced. At Mach 8, laminar flow was produced at the lowest $4.1 \times 10^6/\text{ft}$ condition, transitional flow at the $8.0 \times 10^6/\text{ft}$ condition and turbulent flow at the higher Reynolds numbers.

2. NASA LaRC 20-Inch Mach 6 Air Tunnel Test Parametrics

A short test was also performed in the LaRC 20-Inch Mach 6 Air Tunnel to support the AEDC test. The purpose of this test was to confirm assumptions (to be detailed subsequently) made about thermal properties employed in the thermocouple data reduction process. Runs were performed at Mach 6 over a Reynolds number range of $1.1 \times 10^6/\text{ft}$ to $6.9 \times 10^6/\text{ft}$; the matrix for this test is presented in Table 3.

C. Wind Tunnel Model Design

A 6-inch diameter (0.1524 m) model of the MSL Outer Mold Line (OML)-6 configuration was fabricated from heat-treated 15-5 stainless steel (Figure 2 and Figure 3). As the flight vehicle configuration has been continuously evolving since the design of the test model, the OML-6 test configuration is different from the current OML-12

flight configuration. However, the differences are in the aftbody geometry, and since the primary purpose of this study was to measure forebody heating rates, these differences are not relevant.

The test model was instrumented with 39 Type-E coaxial (chromel-constantan) thermocouples. This type of sensor is routinely used in the AEDC Tunnel 9 facility for aerothermal studies¹⁰. A schematic gage layout is shown in Figure 4. Of the gages, 33 of the 39 were located on the forebody and the remaining gages were located on the aftbody along the centerline. Of the forebody gages, 19 were evenly distributed along the centerline, with additional gages off-centerline in the wind-side stagnation region and outboard on the leeside where the widest growth of the turbulent heating region occurs.

The thermocouples were fitted into the model through pre-drilled holes and fixed with adhesive then sanded carefully to form the required chromel-constantan electrical junctions and to match the surface contours of the model. The shell thickness of the model (and the thermocouple length) was specified at a nominal value of 0.5-in. (slightly less at the corners) in order to ensure that heat-conduction into the model did not violate the semi-infinite assumption (conduction does not reach the interior face) over the length of the AEDC Tunnel 9 test time, which is on the order of 1 second or less.

D. Data Acquisition and Reduction

Thermocouple voltage data from AEDC Tunnel 9 were acquired at a frequency of 500 Hz and analog-filtered at 30 Hz to eliminate 60 Hz analog noise (data from the LaRC 20-Inch Mach 6 Air Tunnel were acquired at 40 Hz). Voltage data were converted to temperatures via the NIST standard calibration formula for Type-E thermocouples. These data were then used to compute heat-transfer rates through a one-dimensional finite-difference numerical method. Descriptions of these methods can be found in Refs. 10-12. As a check on the data reduction process, the test data were reduced using both LaRC and AEDC software tools QCALC¹¹ and 1DHEAT¹² and the results from both codes were in very close agreement.

These conduction analysis methods produce a time-history of the dimensional heat-transfer rate, which is a function of both the free stream conditions and the model surface temperature. Because the free stream conditions in Tunnel 9 vary slightly over the course of the run, and because the rise in model surface temperature can be non-negligible with respect to the stagnation temperature (which drives the convective heating) especially for the high Reynolds number Mach 8 conditions, the heat-transfer rate is not necessarily the ideal parameter with which to

report the test data. Therefore, results are presented herein in terms of the product of the Stanton number times the square-root of the Reynolds number, $St \times (Re_{\infty,D})^{0.5}$, which is defined as:

$$(1) \quad St \times (Re_{\infty,D})^{1/2} = \frac{q}{\rho_{\infty} U_{\infty} \Delta H} \sqrt{\frac{\rho_{\infty} U_{\infty} D}{\mu_{\infty}}}$$

where

$$(2) \quad \Delta H = c_p T_{\infty} + \frac{U_{\infty}^2}{2} - c_p T_w$$

This non-dimensional quantity is very nearly a constant over the course of the run (assuming that the angle of attack is held fixed); the ΔH and q terms balance each other as the wall temperature increases, while the ρ_{∞} and U_{∞} terms account for variations in flow conditions over the run. Also, multiplication by the square-root of the Reynolds number results in a term that has only a very slight dependence on Reynolds number (for laminar flows; for turbulent flows, an exponent of 0.2 on the Reynolds number is frequently employed). When heating distributions are expressed in terms of this parameter, it can be used to correlate laminar heat-flux distributions over the range of test conditions, and transitional/turbulent data can clearly be identified when the values diverge from the lower Reynolds number data, such as shown in Figure 5. It should be noted that this parameter is sometimes defined in other studies using edge conditions instead of free stream conditions for the density and velocity and the adiabatic or reference wall enthalpy instead of the total enthalpy.

E. Wind Tunnel Model Material Properties

The data reduction methods discussed in the previous sections require specification of the thermal properties of the wind tunnel model in order to determine heat-transfer rates from the temperature-time history. Thermal property data can be obtained from several sources (as cited in Refs. 10-12). However the accuracy of these data is hard to assess and the use of different data sets has a significant effect on the resulting heating levels, as shown in the example in Figure 6. The conduction analysis was initially performed using material thermal property data for chromel since the primary material of a thermocouple is chromel. However, the resulting experimental heating levels were found to be well in excess of predicted levels (more than 20% higher for laminar, perfect-gas flow).

These differences suggested a problem with the experimental method which was verified by two independent experimental investigations: 1) thermocouples were installed into stainless steel and chromel plugs on a flat plate adjacent to NIST-traceable heat-flux calorimeters and then bench-tested under a calibrated radiant lamp¹³ and 2) the MSL wind tunnel model was tested in the NASA LaRC 20-Inch Mach 6 Air Tunnel to rule out any facility-related issues such as flow quality, model installation and instrumentation hook-up, signal acquisition, filtering and recording, etc. As a result of these tests it was found that the use of material thermal property curve fits used by AEDC for 17-4 stainless steel provided the best match with the calibrated heat-source, and when data from both AEDC Tunnel 9 and the NASA LaRC 20-Inch Mach 6 Air Tunnel were reduced using these properties, a close match with predictions was obtained. Curve fits for these properties are given in Eqs. (3)-(5). Furthermore, because the calibration study (Ref. 13) revealed a consistent bias of approximately +3% in the coaxial data, the final data generated for this study were post-processed to remove that bias. The reason for the better fit obtained using 17-4 thermal properties has not yet been conclusively determined; it may be possible that the heat-transfer process within the model is dominated by the much larger thermal mass of the model itself or it may be that the available data on the thermal properties of the thermocouple is simply wrong and the actual values are coincidentally closer to those for available for 17-4 stainless steel. In any case, the 17-4 thermal properties given here provide the best fit with both calibration data and predictions, and their use is recommended in the interim until a more detailed investigation into material thermal properties can be conducted.

AEDC 17-4 stainless steel thermal property curve fits:

$$(3) \ (\rho)_m = 7805.7 \left(\frac{kg}{m^3} \right)$$

$$(4) \ (c_p)_m = 409.76 - 5.3809 \times 10^{-2}T + 6.0366 \times 10^{-4} \left(\frac{J}{kg-K} \right)$$

$$(5) \ (k)_m = 11.665 + 1.52078 \times 10^{-2}T \left(\frac{W}{m-K} \right)$$

F. Experimental Uncertainty

The experimental uncertainty of the heat-transfer data is clearly very dependent on the selection of material properties. As shown in the previous section, this uncertainty is on the order of $\pm 10\%$ to 20% . This error source could be lowered, at least in theory, through a more detailed statistically-based study of material properties, but such a study is outside the scope of the MSL project. Separate from this source are uncertainties due to variations in free stream conditions, model angle of attack, and instrumentation precision. For heat-transfer testing with Type-E thermocouples on a blunt configuration such as MSL, an uncertainty of $\pm 6\%$ (not including thermal properties) for these factors is quoted as a standard by AEDC. Although no formal analyses was performed for the LaRC Mach 6 tunnel because the use of thermocouples there is so rare, the flow conditions are more steady than those in Tunnel 9 due to the method of operation, so the uncertainty should be no more than that estimated for Tunnel 9. Taking into account the independent assessment of material thermal properties with a calibrated heat-source, and the generally good agreement with predictions obtained in both wind tunnels, it is recommended that a lower range estimate for material properties uncertainty of $\pm 10\%$ be combined with the quoted AEDC uncertainty of $\pm 6\%$ to give a root-mean-squared uncertainty of $\pm 11.66\%$, which can be rounded up to $\pm 12\%$ for simplicity.

III. □ Computational Method

Flow field computations at the wind tunnel test conditions were performed using the LAURA code^{14,15}. The LAURA (Langley Aerothermodynamic Upwind Relaxation Algorithm) code is a three-dimensional, finite-volume solver that includes perfect-gas, equilibrium, and non-equilibrium chemistry models. The code can be used to solve the inviscid, viscous thin-layer Navier-Stokes, or full Navier-Stokes equations. For the current study the thin-layer model was employed; it was concluded in reference 4 from computations on a similar blunt body that this model provided accurate results for attached forebody flows. Time integration to steady-state in LAURA is accomplished through a point-relaxation scheme. Roe-averaging¹⁶ with Harten's entropy fix¹⁷ and Yee's Symmetric Total Variation Diminishing limiter¹⁸ is used for inviscid fluxes, and a second-order scheme is employed for viscous fluxes. In this study, a perfect-gas model was used for the AEDC and LaRC tunnel conditions with the appropriate gas parameters for either pure N_2 (AEDC Tunnel 9) or air (LaRC 20-Inch Mach 6 Air).

For the AEDC CFD cases, free stream conditions were extracted from the data set for that run at the time at which the specified angle-of-attack was reached because the free stream conditions do vary over the length of a run. For the wall boundary condition, a uniform temperature over the body equal to that recorded at the nose gage (C10)

at the specified time during the run was used. For the LaRC 20-Inch Mach 6 Air Wind Tunnel cases, free stream conditions do not vary significantly over the length of the run, so the nominal conditions in Table 3 could be used. The wall temperature boundary condition was specified in the same manner as for the AEDC CFD cases.

Structured, finite-volume, multiple-block forebody grids with a singularity-free nose were employed for the computations. Grid adaptation was performed (as per the method detailed in reference 15) to align the grid with the bow shock and to produce nominal wall cell Reynolds numbers on the order of 1.

Laminar computations were performed for AEDC and LaRC tunnel cases. Turbulent computations were performed for several cases using the algebraic Cebici-Smith turbulence model (the algebraic Baldwin-Lomax model was used for a few selected AEDC cases and found to produce only slightly different results for these perfect-gas conditions). While it is recognized that more sophisticated turbulent models exist, different models can produce very different results (e.g. reference 19) and the validation status of any and all turbulence models for hypersonic flow over a given vehicle type is debatable. Algebraic models are the standard being used for MSL flight database development because they are computationally fast and stable, and as will be shown subsequently, the accuracy of algebraic model turbulent predictions on the forebody, at least for the conditions under consideration, is generally as good as that of the laminar predictions.

IV. Results and Analysis

A. AEDC Tunnel 9 Data

The AEDC test was conducted in a continuous-pitch mode, and so heating data were obtained over the entire angle-of-attack range of each run (~26 deg. at Mach 10 or ~10 deg. at Mach 8). Values at a specific angle of attack were extracted from the data set by averaging over a time-interval encompassing ± 0.5 deg from the nominal value. This data set is far larger than can be presented herein, so for the purposes of this report, this discussion will focus on the forebody $\alpha = 16$ deg data since that is the current trim-angle for flight.

A sampling of the data obtained over the complete pitch-sweep range is given in Figure 7 and Figure 8 for the Mach 10 conditions and in Figure 9 and Figure 10 for the Mach 8 conditions in which data are presented for both low and high Reynolds number runs in each nozzle. The Mach 10 data shown indicate laminar behavior for all α at the $Re_\infty = 1 \times 10^6/\text{ft}$ condition and transitional or fully-turbulent behavior on the leeside ($x/R > 0$) at the $Re_\infty = 19 \times 10^6/\text{ft}$ condition depending on α . For the Mach 8 Reynolds number cases shown, the data appear to be

transitional or fully-turbulent on the leeside for all α at both Reynolds numbers except possibly at the lowest α -values at the $Re_\infty = 8 \times 10^6/\text{ft}$ condition. Additionally, the wind-side data at the high Reynolds number Mach 8 conditions also appear to be transitional or turbulent.

Although the purpose of this study was not to formulate or validate transition criteria, some insight into the transitional/turbulent behavior of the data can be gained by examining boundary-layer parameters such as Re_θ and Re_θ/M_e . Computed values of these parameters for $\alpha = 16$ at the Mach 10 and Mach 8 nozzle conditions are plotted in Figure 11 and Figure 12. Previous studies⁷ have indicated that transition occurs between values of 200 to 400 for Re_θ/M_e , while the design specification³ for the MSL program is to assume turbulent flow in flight for values of Re_θ greater than 200, which occurs well before the peak-heating point on current design trajectories. Conditions in both nozzles exceed these values – by a great deal in the Mach 8 nozzle – which provides evidence that the data at higher Reynolds numbers can be interpreted as fully-turbulent.

Comparisons between the tunnel data and CFD predictions along the centerline of the model are presented in Figure 13 to Figure 18 for the Mach 10 conditions and in Figure 19 to Figure 24 for the Mach 8 conditions. Error bars on the wind tunnel data in these figures correspond to the $\pm 12\%$ estimate previously discussed. When available, data from repeat runs are also plotted, although the error bars are shown for only one of the data sets in order to make the plots readable.

Both laminar and, where appropriate, turbulent predictions are shown in these figures. The turbulent predictions were made assuming fully-developed turbulent flow over the entire forebody, whereas in the actual test, fully-developed turbulent flow was only produced over portions of the leeside of the vehicle at Mach 10 and over portions of the wind-side and most of the leeside at Mach 8. Although it would have been possible to set a transition onset location in the algebraic turbulence models used for the predictions in order to better match the observed range of boundary-layer behavior, this option was not employed in the current analysis since the transition locations were not known *a priori*. In theory, it would be possible to develop a transition onset criterion from the current data set, and then use that result to specify transition onset for the computational methods, but such a step was beyond the scope of the current study.

The data from the four lowest Mach 10 Reynolds numbers cases appeared to all be laminar, and for these cases the predictions and data matched to within much less than the $\pm 12\%$ experimental uncertainty for almost all data points. The leeside transitional data for the next-to-highest case ($Re_\infty = 15 \times 10^6/\text{ft}$) were higher than the laminar

prediction, and for the leeward side at the highest case ($Re_\infty = 19 \times 10^6/\text{ft}$) the turbulent prediction matched the leeward side centerline data. For these two cases, there were also slight indications of a non-laminar heating augmentation in the wind-side stagnation region such as was noted in Ref 7.

The Mach 8 comparisons are more difficult to interpret, because it is unclear whether any of the conditions provided a completely laminar case. If the two lowest Reynolds cases of $Re_\infty = 4 \times 10^6/\text{ft}$ and $Re_\infty = 8 \times 10^6/\text{ft}$ were laminar, then the differences between measurement and prediction are clearly greater than observed for the Mach 10 laminar cases, whereas if these data were transitional, the comparisons may be reasonable. For the higher Reynolds number Mach 8 cases ($Re_\infty = 16 \times 10^6/\text{ft}$ to $Re_\infty = 49 \times 10^6/\text{ft}$), the Re_θ/M_e and Re_θ values shown in Figure 12, as well as the shape of the experimental centerline heating distributions, clearly suggested that these data were turbulent. In fact, the two highest Reynolds number cases ($Re_\infty = 31 \times 10^6/\text{ft}$ and $Re_\infty = 49 \times 10^6/\text{ft}$) appeared to be fully turbulent over the entire body, which may be the first experimental data set in which such behavior has been observed for a large-angle, blunted sphere-cone geometry such as MSL. For these four highest Reynolds number Mach 8 cases, the agreement was better than the lower Reynolds number cases, with the turbulent predictions falling within the $\pm 12\%$ experimental uncertainty from the tunnel data.

As with the Mach 10 comparisons, the Mach 8 comparisons also showed that measured heating values in the wind-side stagnation region exhibited a non-laminar heating augmentation that was not predicted by the computations. This result suggests a deficiency in the turbulence models used for the study. However, the methodology employed for flight heating predictions for the MSL vehicle is to perform fully-turbulent computations over the entire forebody; therefore since the augmentation observed in the data is small, it is bounded by the flight predictions and thus does not appear to be a design concern.

B. NASA LaRC 20-Inch Mach 6 Air Tunnel Heating Data and CFD Comparisons

Results from the LaRC 20-Inch Mach 6 Air Tunnel test are compared with laminar predictions in Figure 25 to Figure 29. Only laminar predictions are shown for these cases since the model appeared to remain laminar for all test conditions except at the highest Reynolds number of $Re_\infty = 6.9 \times 10^6/\text{ft}$ where the flow became transitional on the leeward side just before the corner. Centerline Re_θ and Re_θ/M_e values for these cases are plotted in Figure 30; these values are in the same range as the lower AEDC Tunnel 9 Mach 10 nozzle conditions, in which laminar flow was also observed. In general, predictions and wind tunnel data were again within the estimated $\pm 12\%$ experimental

uncertainty although the stagnation region augmentation was more noticeable than in the AEDC Tunnel 9 data, and the predictions were consistently lower than the data at the nose of the model. One possible reason for this under-prediction is that the run time in the LaRC 20-Inch Mach 6 Air Tunnel was longer than that in the AEDC Tunnel 9 (~5 seconds as compared to ~1 second) due to the length of time required to inject the model into the test section. The wind tunnel model wall thickness was only designed to satisfy the semi-infinite conduction assumption (i.e. the temperature rise within the model does not reach the back-face) in Tunnel 9, and so the longer Mach 6 test time may have introduced errors into the analysis. As a result of this study, the operating sequence for thermocouple testing in this facility has been modified to permit faster model injection and thus reduce the total test time to avoid violating the semi-infinite assumption.

V. □ Summary and Conclusions

An experimental investigation of aerodynamic heating to the forebody of the MSL entry vehicle was conducted in the Mach 10 and Mach 8 nozzles of AEDC Tunnel 9 and laminar, transitional, and turbulent data were obtained. The purpose of this test was to determine the accuracy with which the computational tools being used in the design of the MSL vehicle could predict turbulent heating levels in an environment free from the uncertainties produced in a high-enthalpy, non-equilibrium impulse facility.

Heating data were obtained using coaxial thermocouples and comparisons were made with laminar and turbulent CFD predictions. The measurements and predictions were found to compare to within the estimated $\pm 12\%$ experimental uncertainty for cases where either fully-laminar or fully-turbulent flow was produced except at the two lowest Reynolds numbers in the Mach 8 nozzle of Tunnel 9, where it was unclear whether the data were transitional or if the comparisons revealed a bias, and in some of the higher Reynolds number Mach 8 and Mach 10 data where a non-laminar augmentation of the data was observed in the wind-side stagnation region.

These good comparisons were obtained only after the effects of the model material thermal properties were investigated and it was concluded that original properties used were probably incorrect. Preliminary recommendations for a new set of thermal properties for use in thermocouple data reduction were made based on these results.

To support the AEDC Tunnel 9 test, a short test was also performed in the LaRC 20-Inch Mach 6 Air Tunnel to validate the use of these thermal properties. Predictions for the Mach 6 conditions were also generally within the

±12% experimental uncertainty, although in some regions the agreement was not as good, probably due to violation of the semi-infinite wall assumption due to longer run times in this facility.

VI. □ References

¹Lockwood, M. K., “Introduction: Mars Science Laboratory: The Next Generation of Mars Landers,” *Journal of Spacecraft and Rockets*, Vol. 43., No. 2, March-April 2006, p. 257.

²Lockwood, M. K., Powell, R. W., Sutton, K., Prabhu, R. K., Graves, C. A., Epp, C. D., and Carman, G. L., “Entry Vehicle Configurations and Performance for the Mars Smart Lander,” *Journal of Spacecraft and Rockets*, Vol. 43, No. 2, March-April 2006, pp. 258-269.

³Edquist, K. T. “Aerothermodynamic Environments Definition for the Mars Science Laboratory Entry Capsule,” AIAA Paper 2007-1206, 45th AIAA Aerospace Sciences Meeting and Exhibit, Reno, NV, Jan. 8-11, 2007.

⁴Hollis, B. R., and Liechty, D. S., “Transition Due to Heat-Shield Cavities on a Mars Entry Vehicle,” *Journal of Spacecraft and Rockets*, Vol. 43., No. 2, March-April 2006, pp. 354-366.

⁵Liechty, D. S., Hollis, B. R., and Edquist, K. T., “Mars Science Laboratory Experimental Aerothermodynamics with Effects of Cavities and Control Surfaces,” *Journal of Spacecraft and Rockets*, Vol. 43., No. 2, March-April 2006, pp. 340-353.

⁶Wright, M. J., Olejniczak, J. Brown, J. L., Hornung, H. G., and Edquist, K. T., “Modeling of Shock Tunnel Aeroheating Data on the Mars Science Laboratory Aeroshell,” *Journal of Thermophysics and Heat Transfer*, Vol. 20, No. 4, October-December 2006, pp. 641-646.

⁷Hollis, B. R., Liechty, D. S., Wright, M. J., Holden, M. S., Wadhams, T. P., MacLean, M. and Dyakonov, A., “Transition Onset and Turbulent Aeroheating Measurements on the Mars Science Laboratory Entry Vehicle,” AIAA Paper 2005-1437, January, 2005.

⁸Marren, D., and Lafferty, J., “The AEDC Hypervelocity Wind Tunnel 9,” *Advanced Hypersonic Test Facilities, Progress in Aeronautics and Astronautics*, Vol. 198, American Institute of Aeronautics and Astronautics, Reston, VA, 2002, pp. 467-477.

⁹Micol, J. R. “Langley Aerothermodynamic Facilities Complex: Enhancements and Testing Capabilities,” AIAA Paper 98-0147, January 1998.

¹⁰Hedlund, E. R., Hill, J. A. F., Ragsdale, W. C., and Voisinet, R. L. P., “Heat Transfer Testing in the NSWC Hypervelocity Wind Tunnel Utilizing Co-Axial Surface Thermocouples,” Naval Surface Weapons Center - NSWC-MP 80-151, March 1980.

¹¹Boyd, C. F., and Howell, A., “Numerical Investigation of One-Dimensional Heat-Flux Calculations,” Naval Surface Warfare Center NSWCDD/TR-94/114, October 1994.

¹²Hollis, B. R., “User’s Manual for the One-Dimensional Hypersonic Aero-Thermodynamic (1DHEAT) Data Reduction Code,” NASA CR-4691, August 1995.

- ¹³Coblish, J. C., "Aerothermal Measurement Improvements Using Coaxial Thermocouples at AEDC Hypervelocity Wind Tunnel No. 9," AIAA Paper 2007-1467, 45th AIAA Aerospace Sciences Meeting and Exhibit, Reno, NV, Jan. 8-11, 2007.
- ¹⁴Gnoffo, P. A., "An Upwind-Biased, Point-Implicit Algorithm for Viscous, Compressible Perfect-Gas Flows," NASA TP-2953, February 1990.
- ¹⁵Cheatwood, F. M., and Gnoffo, P. A., "User's Manual for the Langley Aerothermodynamic Upwind Relaxation Algorithm (LAURA)," NASA TM 4674, April, 1996.
- ¹⁶Roe, P. L., "Approximate Riemann Solvers, Parameter Vectors and Difference Schemes," *Journal of Computational Physics*, Vol. 43, No. 2, 1981, pp. 357-372.
- ¹⁷Harten, A., "High Resolution Schemes for Hyperbolic Conservation Laws," *Journal of Computational Physics*, Vol. 49, No. 3, 1983, pp. 357-393.
- ¹⁸Yee, H. C., "On Symmetric and Upwind TVD Schemes," NASA TM 88325, 1990.
- ¹⁹Brown, J. L., "Turbulence Model Validation for Hypersonic Flows," AIAA Paper 2002-3308, 8th AIAA/ASME Joint Thermophysics and Heat Transfer Conference, St. Louis, MO. June 24-26, 2002.

Table 1. Comparison of Mars Entry Vehicles

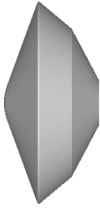


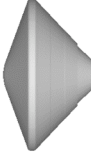
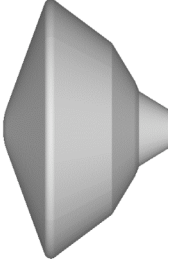
	Viking 1 & 2	Pathfinder	MER A & B	Phoenix	MSL
Configuration					
Diameter, m	3.5	2.65	2.65	2.65	4.5
Entry Mass, kg	930	585	840	602	> 3000
Landed Mass, kg	603	360	539	364	> 1700
Relative Entry Vel., km/s	4.5/4.42	7.6	5.5	5.9	> 5.5
Relative Entry Angle, deg	-17.6	-13.8	-11.5	-13	-15.2
Ballistic Coefficient, kg/m ²	63.7	62.3	89.8	65	> 140
Turbulent at Peak Heating?	No	No	No	No	Yes
Peak Heat Flux, W/cm ²	24	115	54	56	> 200
Hypersonic α , deg	-11.2	0	0	0	-15.5
Hypersonic L/D	0.18	0	0	0	0.24

Table 2. AEDC Tunnel 9 Run Matrix (nominal run-averaged conditions)

Run	Re_∞ (1/ft)	M_∞	P_∞ (Pa)	T_∞ (K)	ρ_∞ (kg/m ³)	U_∞ (m/s)	ΔH (MJ/kg)	α (deg)
3020	1.85E+06	9.56	285.1	58.1	0.0165	1486.3	0.853	0 - 26
3021	1.18E+06	9.47	167.9	54.8	0.0103	1428.0	0.765	0 - 26
3022	4.62E+06	9.80	656.1	54.4	0.0406	1474.9	0.832	0 - 26
3023	8.61E+06	10.03	1068.3	51.9	0.0694	1472.5	0.826	0 - 26
3024	1.46E+07	10.22	1696.2	50.2	0.1139	1475.5	0.829	0 - 20
3025	1.91E+07	10.32	2068.1	48.3	0.1444	1461.8	0.807	0 - 18
3026	1.85E+07	10.31	2079.3	49.5	0.1416	1479.2	0.833	5 - 24
3027	8.03E+06	7.43	2302.3	74.6	0.1040	1308.8	0.622	0 - 26
3028	4.13E+06	7.41	1162.5	73.5	0.0533	1294.2	0.602	0 - 26
3029	1.59E+07	7.64	4988.8	80.7	0.2082	1398.3	0.750	0 - 26
3030	2.16E+07	7.77	6158.7	76.6	0.2709	1386.0	0.728	0 - 25
3042	8.52E+06	7.45	2366.9	73.1	0.1091	1298.6	0.607	0
3043	1.65E+07	7.65	4470.0	73.2	0.2059	1334.0	0.654	0
3044	2.15E+07	7.80	5407.0	70.4	0.2589	1333.0	0.650	0
3045	4.50E+07	7.93	11824.6	73.4	0.5426	1383.0	0.721	0
3047	3.04E+07	7.75	8231.8	73.8	0.3760	1356.4	0.685	16
3048	4.96E+07	7.98	11918.6	69.3	0.5792	1350.9	0.673	16
3049	1.61E+07	7.64	4968.0	79.8	0.2097	1391.7	0.739	8 - 19
3050	1.65E+07	7.65	5078.3	79.8	0.2145	1391.8	0.740	12 - 22
3051	2.18E+07	7.77	6235.2	76.6	0.2742	1386.8	0.729	8 - 19
3052	2.23E+07	7.79	5966.0	73.4	0.2739	1359.1	0.688	12 - 22
3053	3.06E+07	7.75	7989.6	71.9	0.3742	1339.3	0.660	9 - 20

Table 3. LaRC 20-Inch Mach 6 Air Tunnel Run Matrix

Run	Re_∞ (1/ft)	M_∞	P_∞ (Pa)	T_∞ (K)	ρ_∞ (kg/m ³)	U_∞ (m/s)	ΔH (MJ/kg)	α (deg)
1	6.92E+06	6.04	1939	63.2	0.1073	959.1	0.214	16
2	5.85E+06	6.03	1633	62.9	0.0906	956.4	0.211	16
3	4.02E+06	6.01	1100	61.9	0.0620	945.7	0.200	16
4	2.13E+06	5.96	584	61.8	0.0329	939.4	0.194	16
5	1.08E+06	5.89	297	61.3	0.0169	924.3	0.179	16
6	1.39E+06	5.92	381	61.6	0.0216	931.4	0.186	16

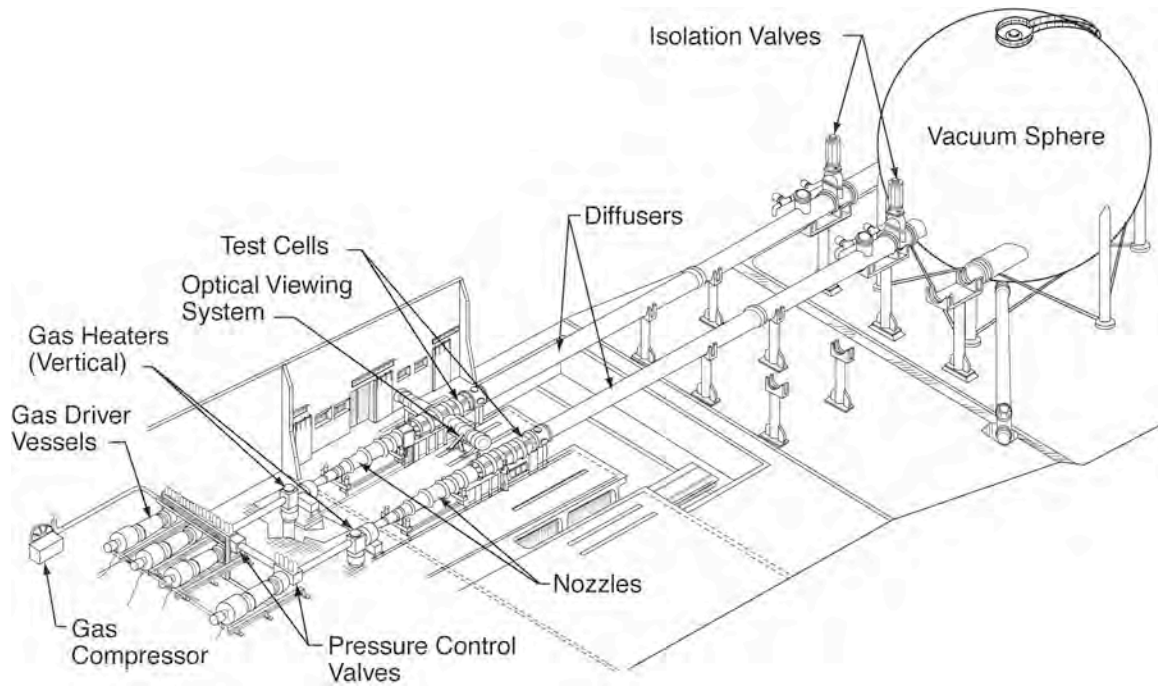


Figure 1. AEDC Tunnel 9 Schematic



Figure 2. Close-up view of MSL model in NASA LaRC 20-Inch Mach 6 Air Tunnel (retracted into model box)

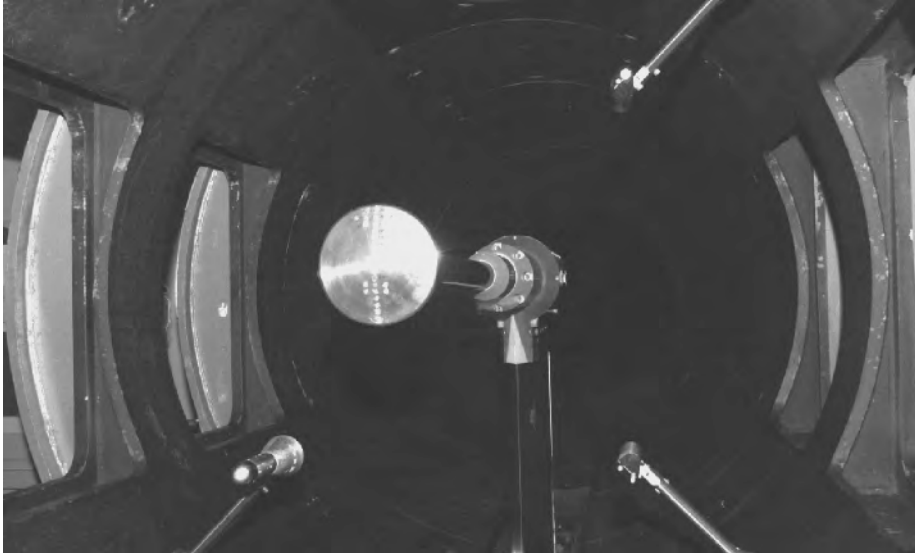


Figure 3. MSL Model installed in AEDC Tunnel 9

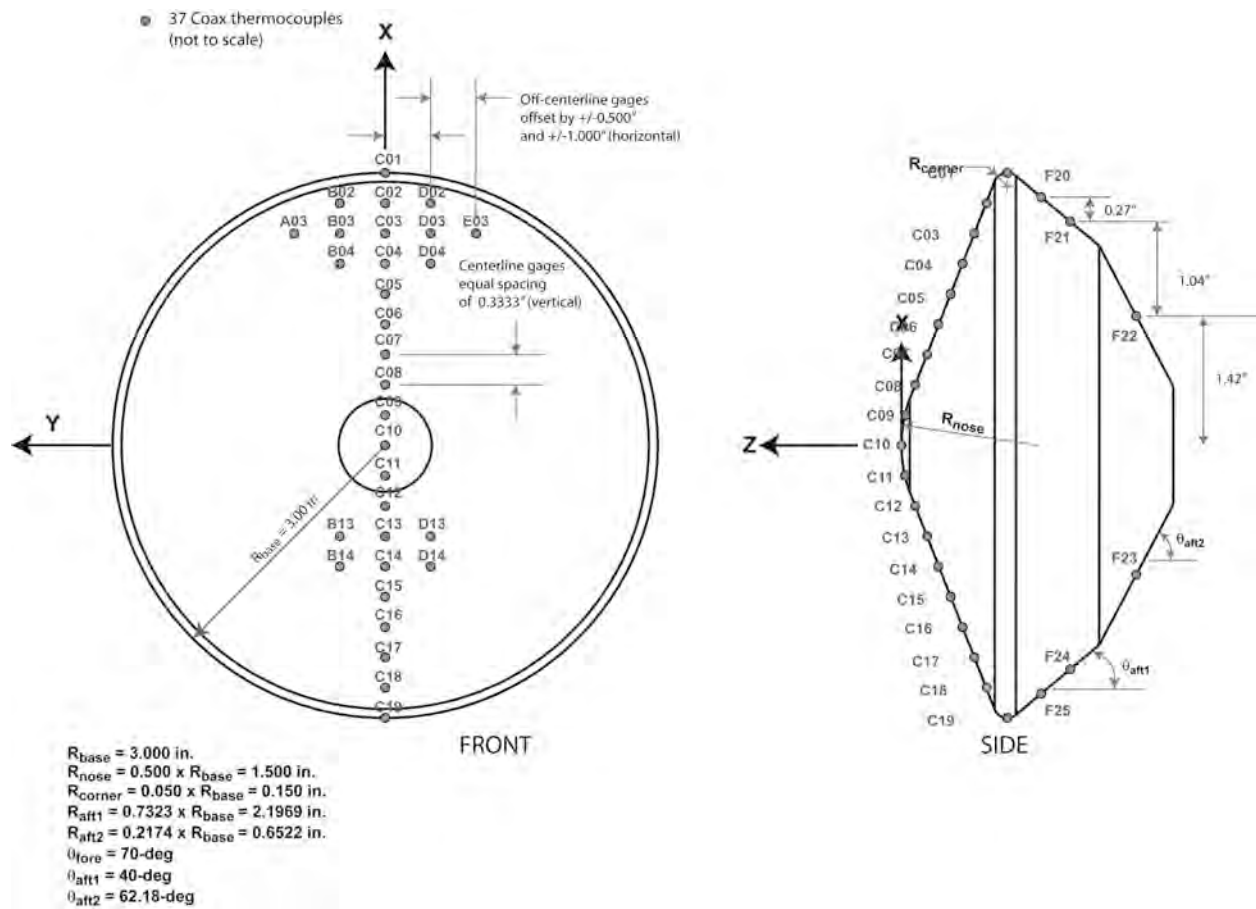


Figure 4. MSL model dimensions and thermocouple layout

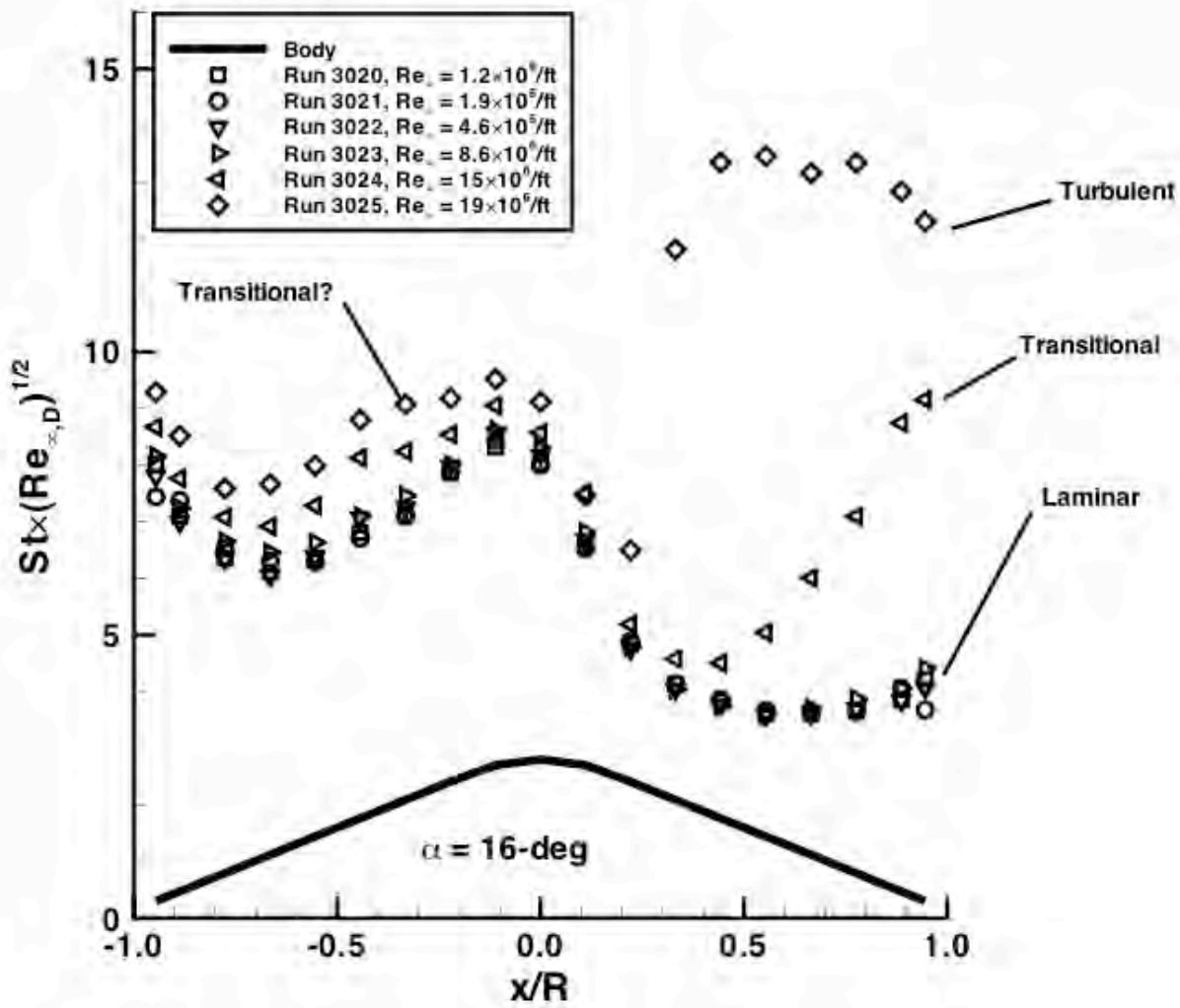


Figure 5. Correlation of centerline heating distribution vs. free stream Reynolds number

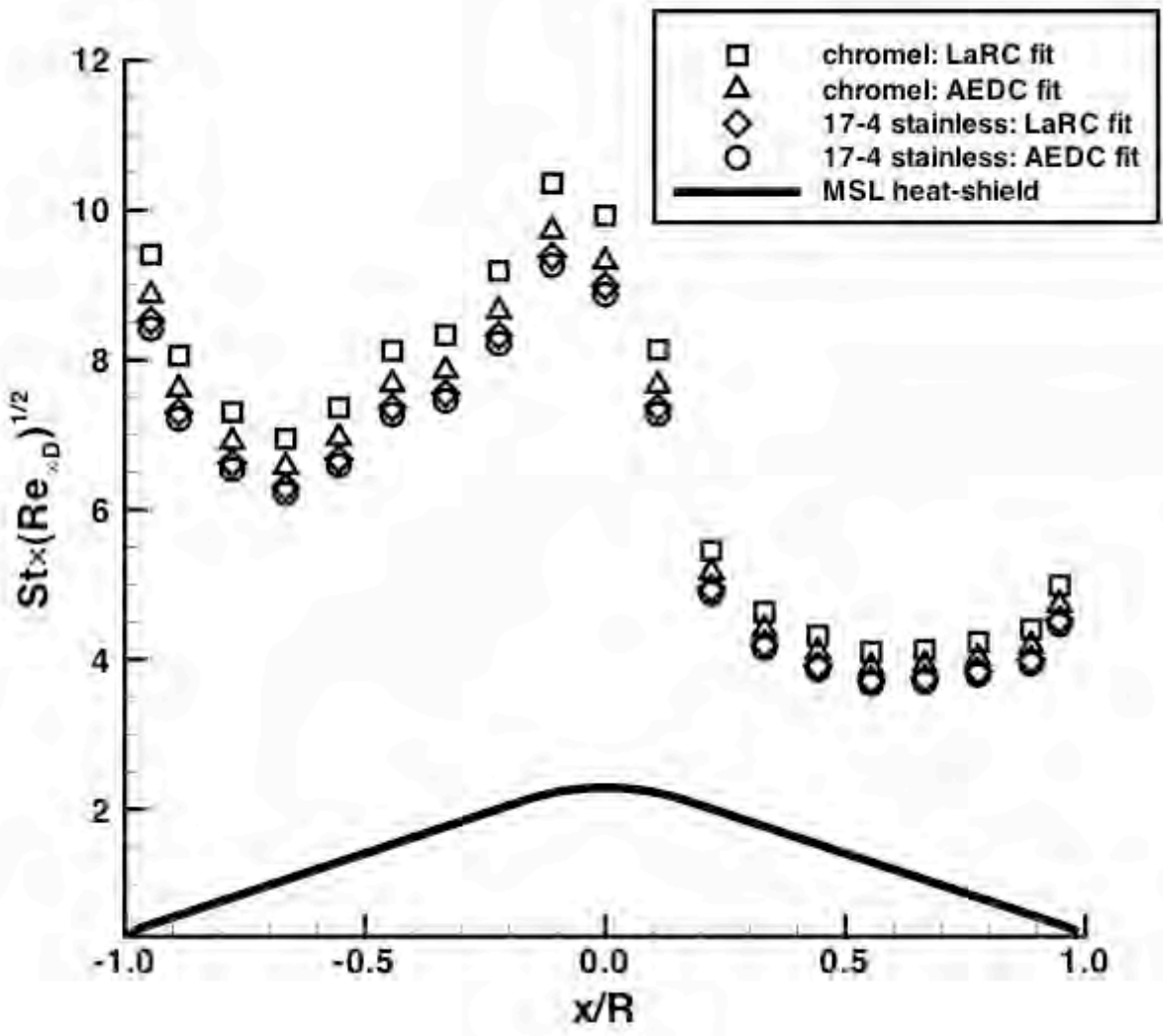


Figure 6. Variation in heating due to choice of thermal properties used in data reduction

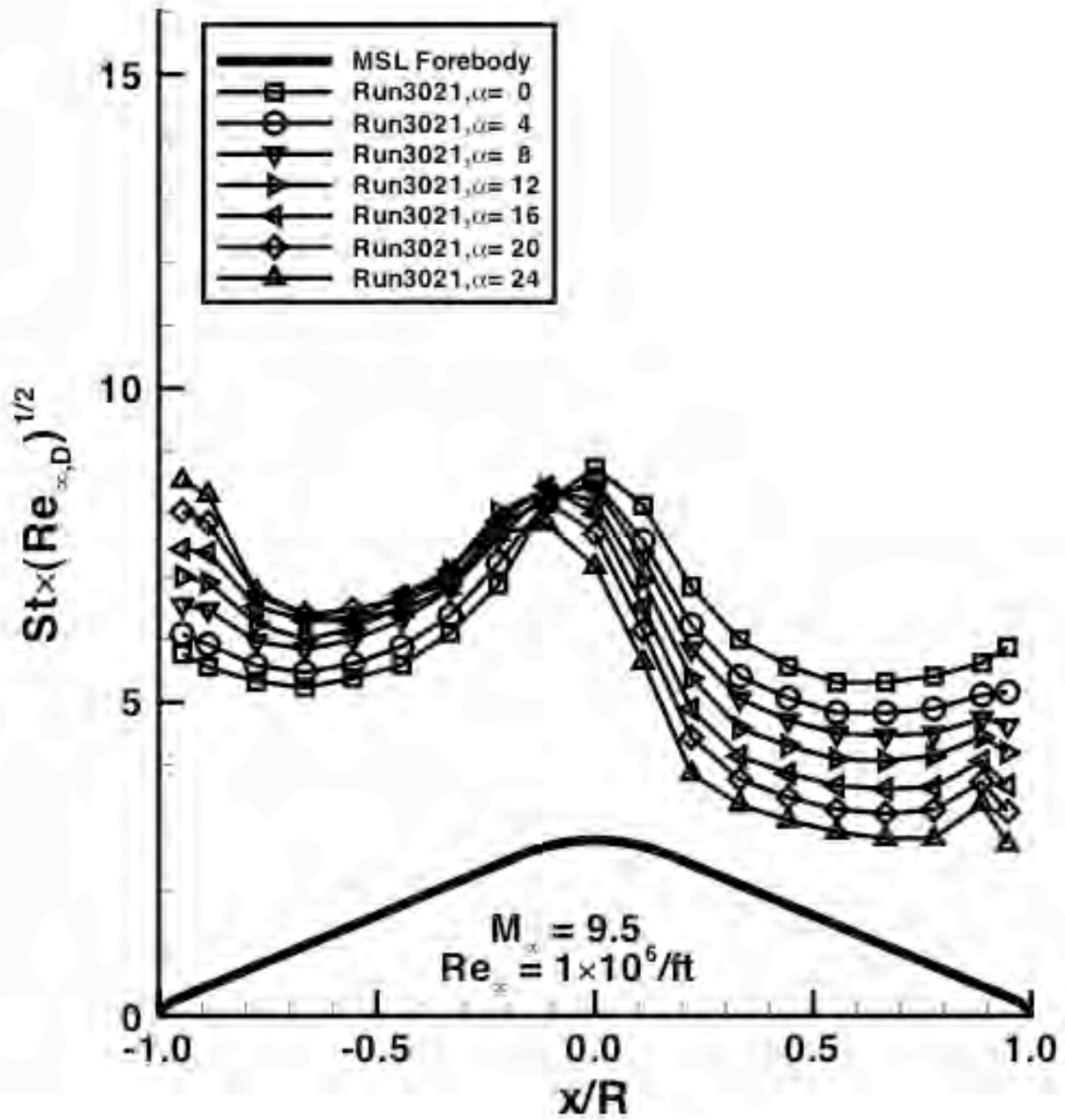


Figure 7. Angle-of-attack effects, Mach 10 nozzle, $Re_{\infty}=1 \times 10^6/ft$

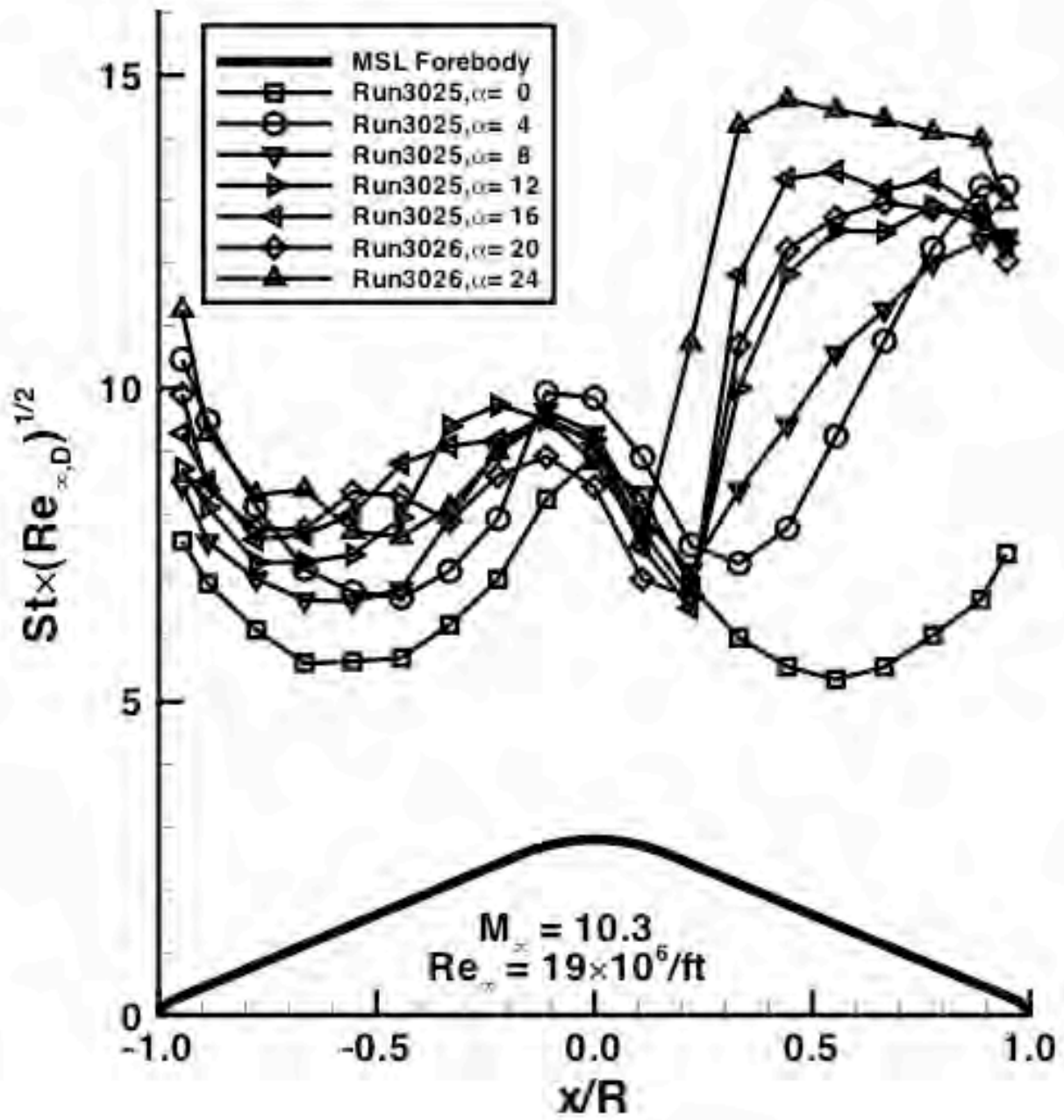


Figure 8. Angle-of-attack effects, Mach 10 nozzle, $Re_\infty = 19 \times 10^6 / ft$

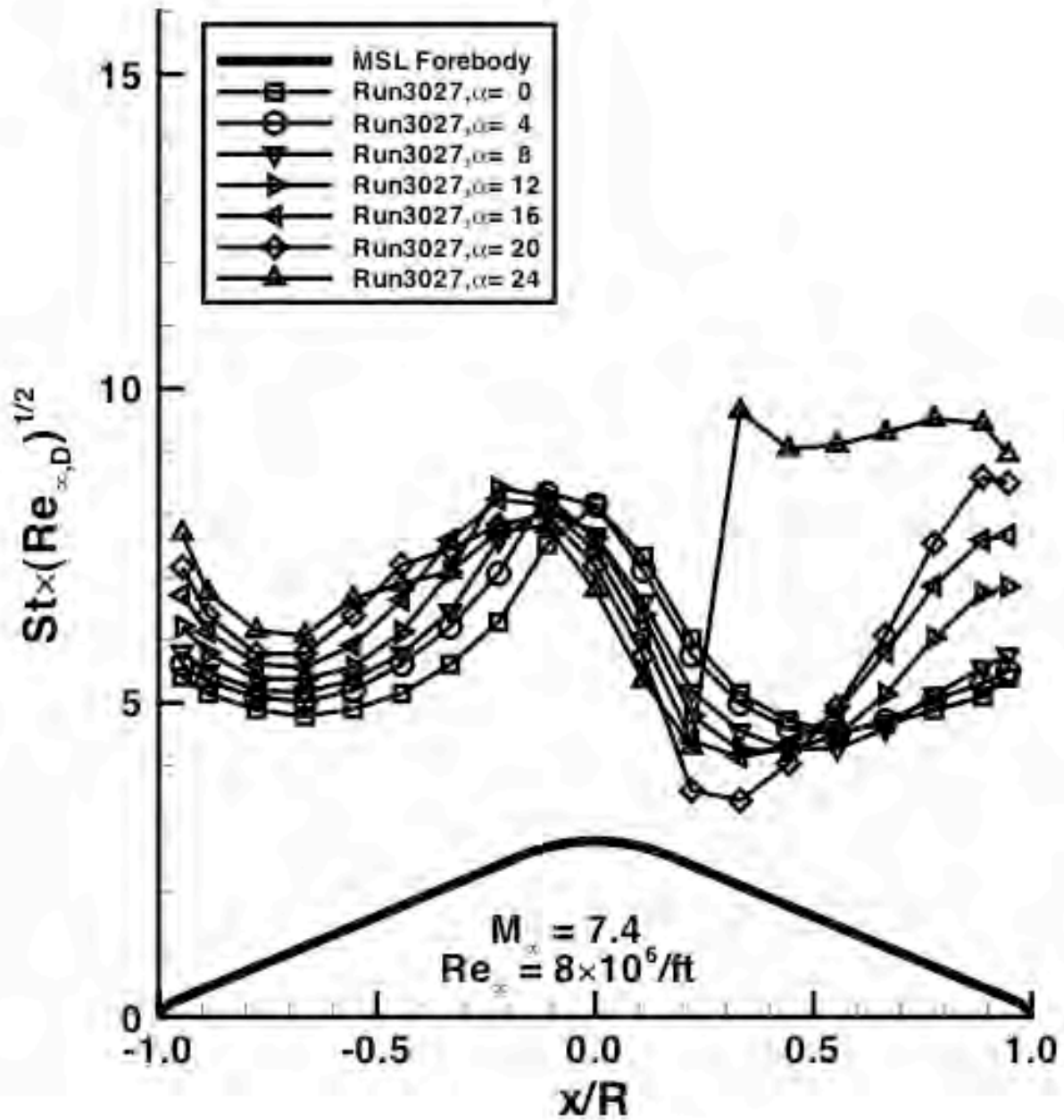


Figure 9. Angle-of-attack effects, Mach 8 nozzle, $Re_\infty = 8 \times 10^6 / ft$

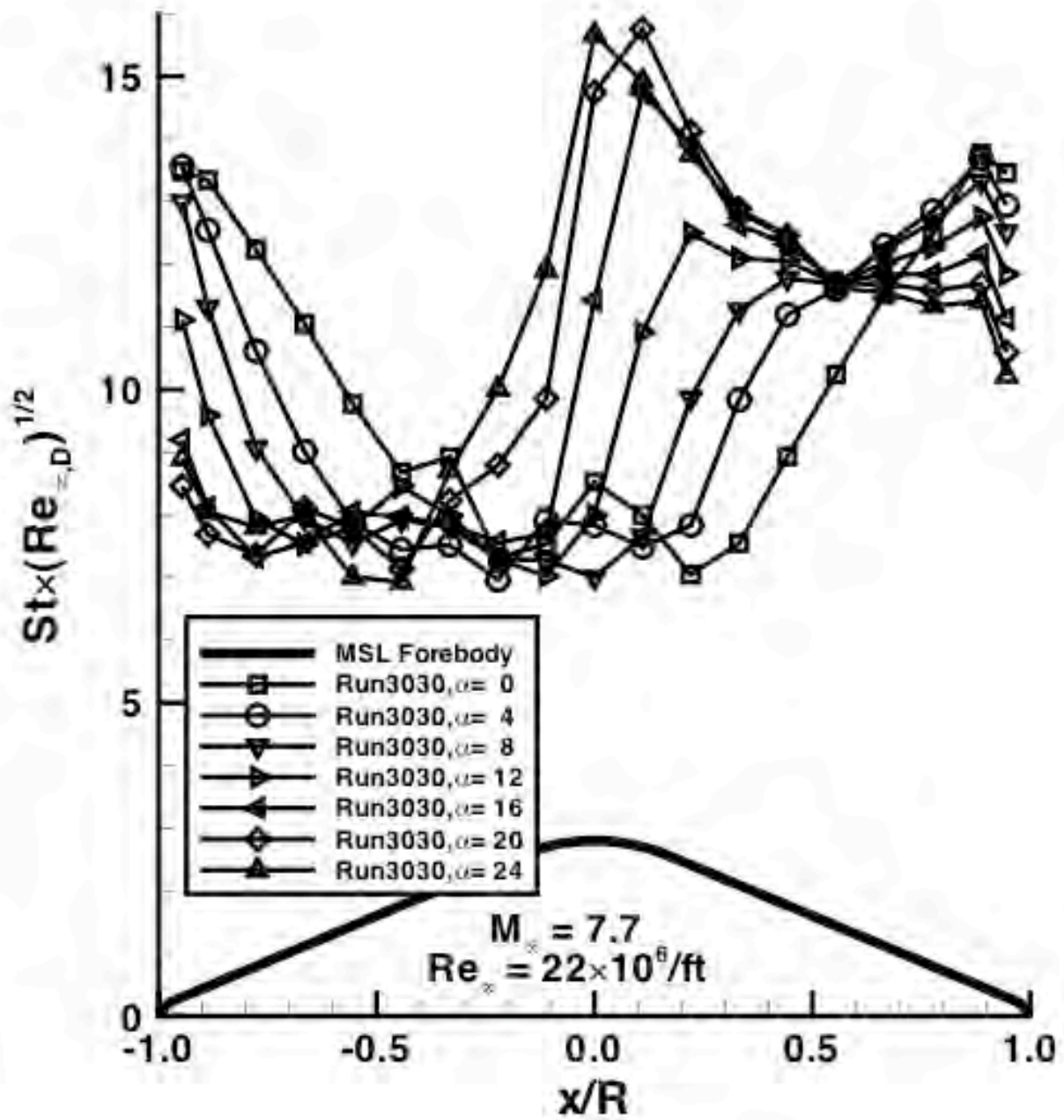


Figure 10. Angle-of-attack effects, Mach 8 nozzle, $Re_\infty = 22 \times 10^6 / ft$

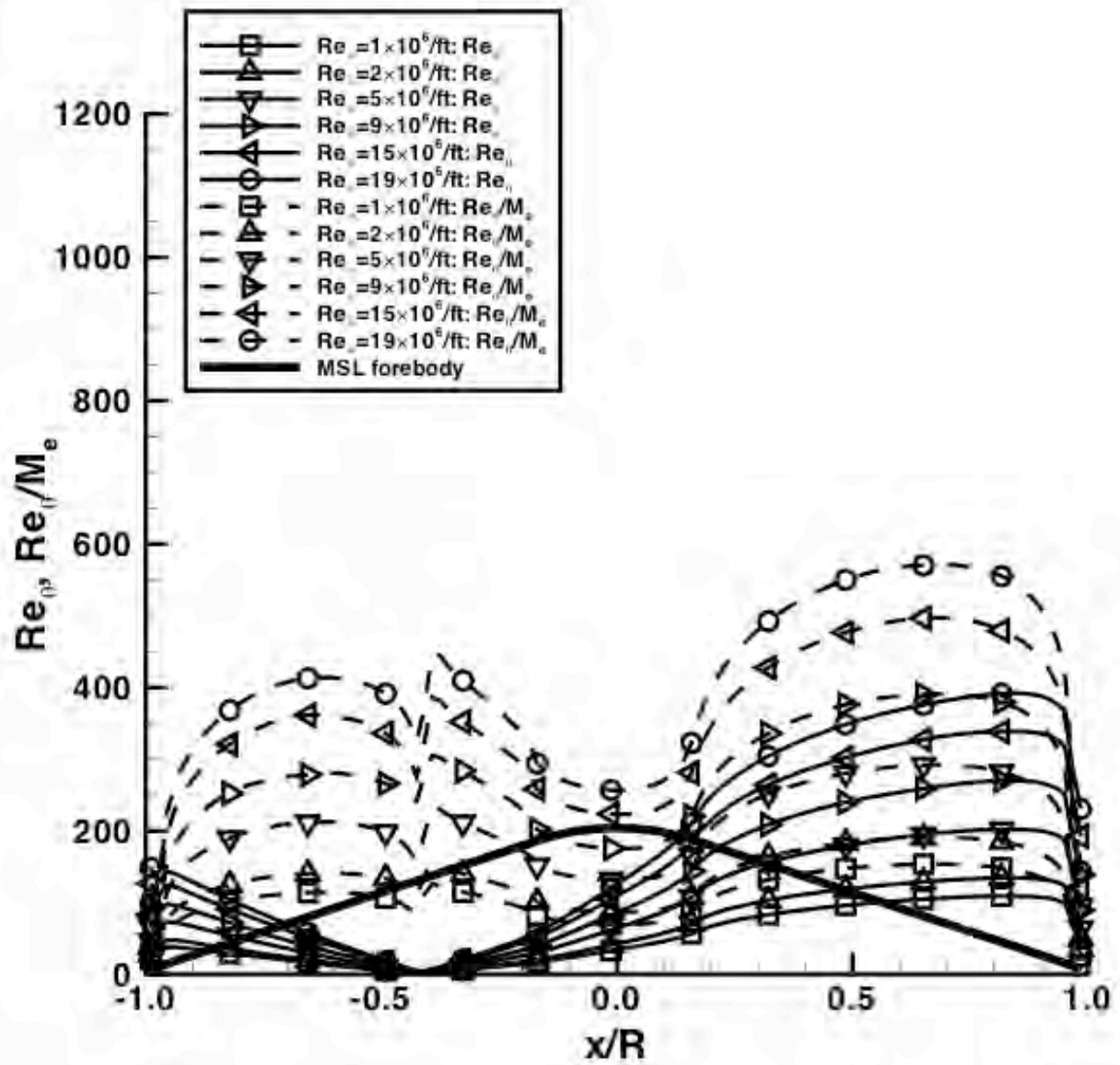


Figure 11. Boundary-layer parameters for AEDC Tunnel 9 Mach 10 nozzle conditions

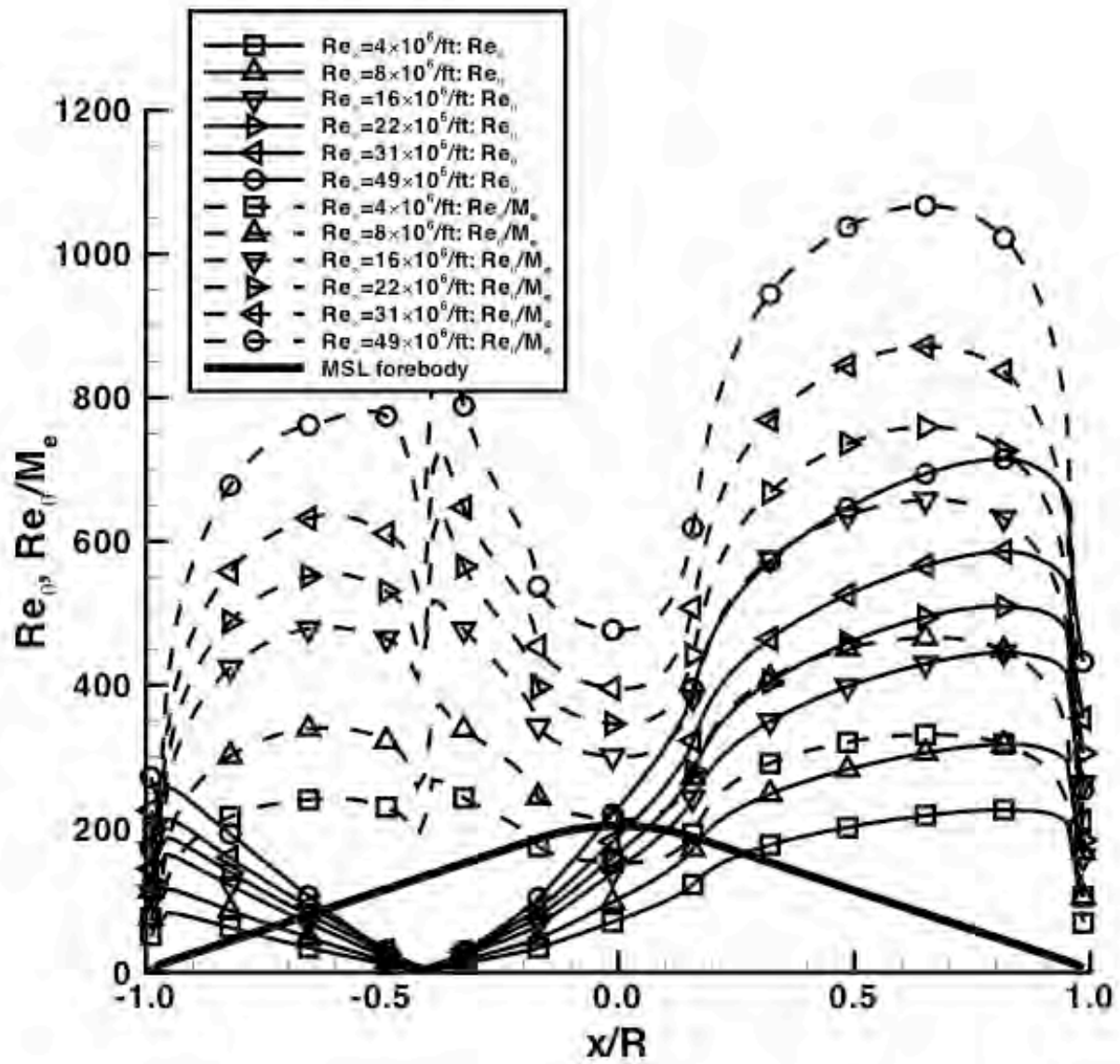


Figure 12. Boundary-layer parameters for AEDC Tunnel 9 Mach 8 nozzle conditions

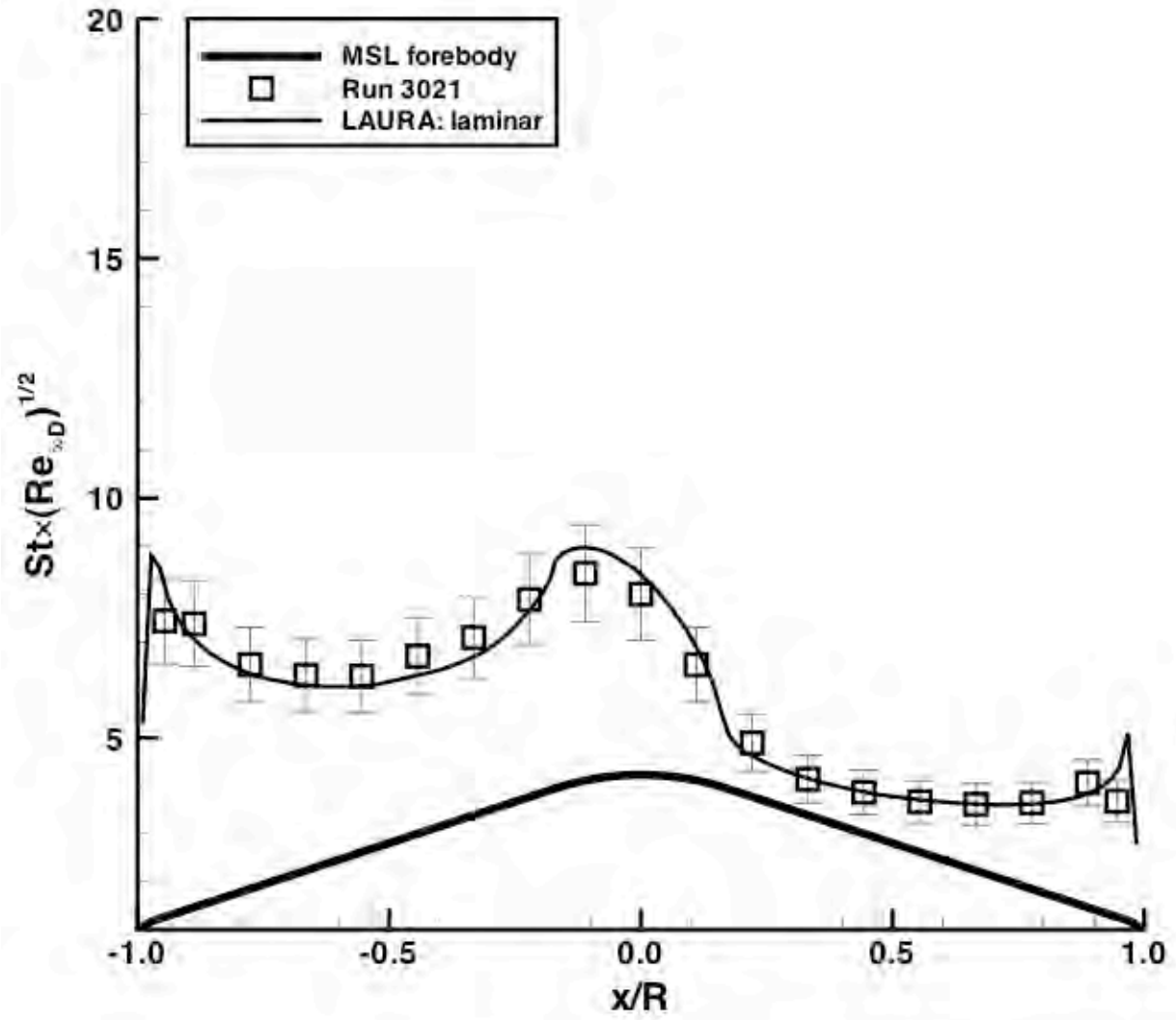


Figure 13. Comparison for Mach 10, $Re_\infty=1.2 \times 10^6/\text{ft}$, $\alpha=16$ deg

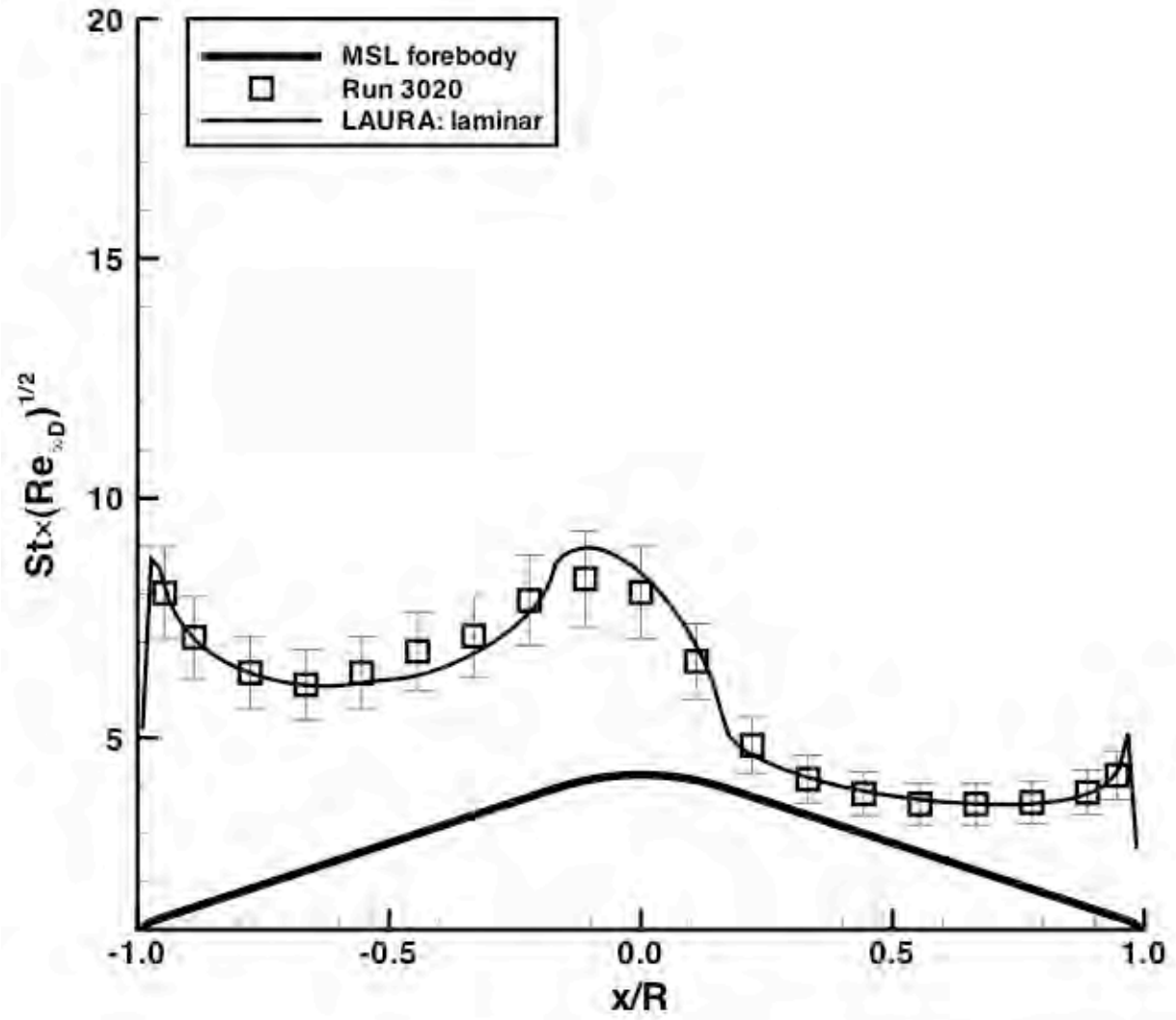


Figure 14. Comparison for Mach 10, $Re_x=1.8 \times 10^6/ft$, $\alpha=16$ deg

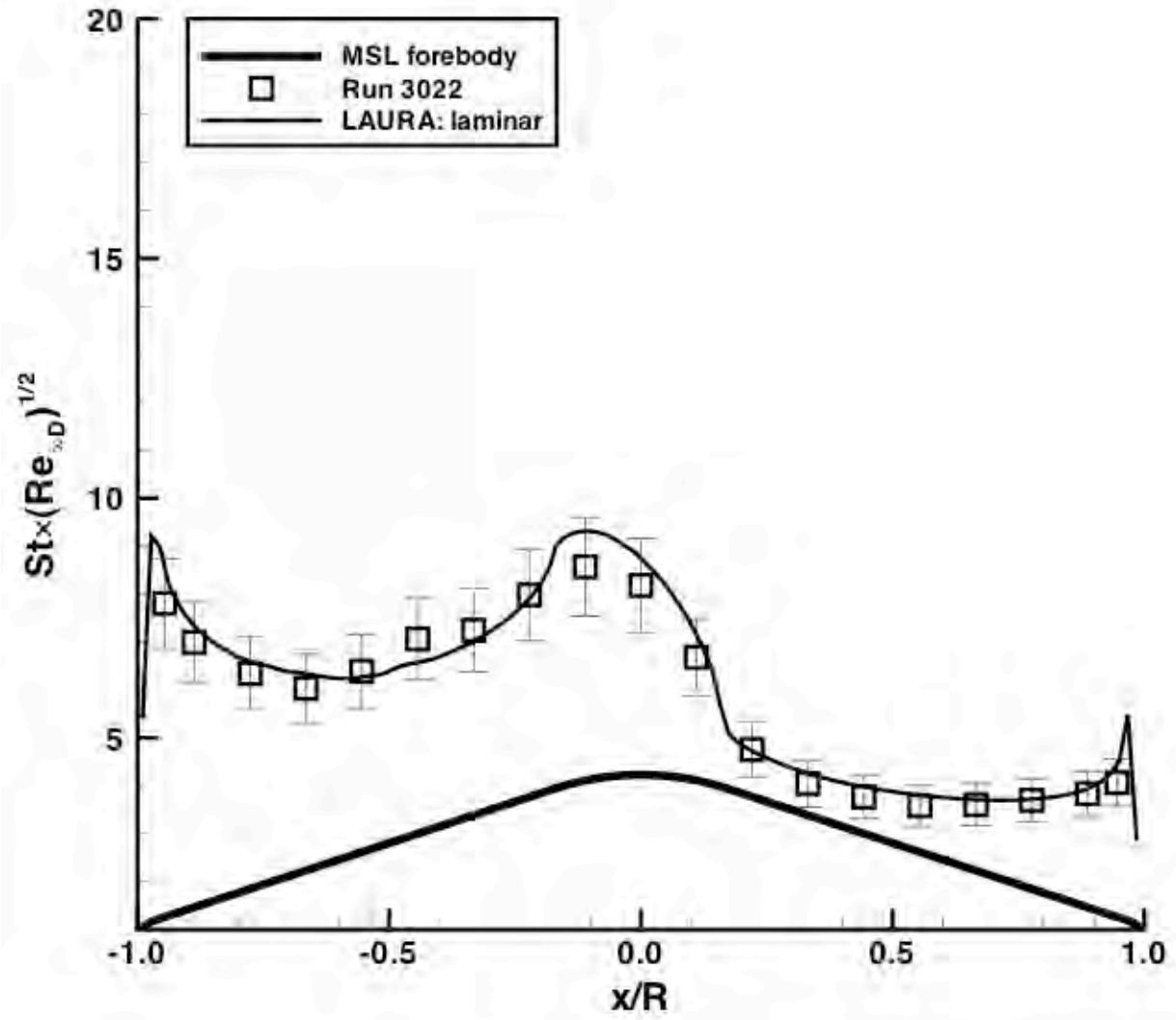


Figure 15. Comparison for Mach 10, $Re_x=4.6 \times 10^6/ft$, $\alpha=16$ deg

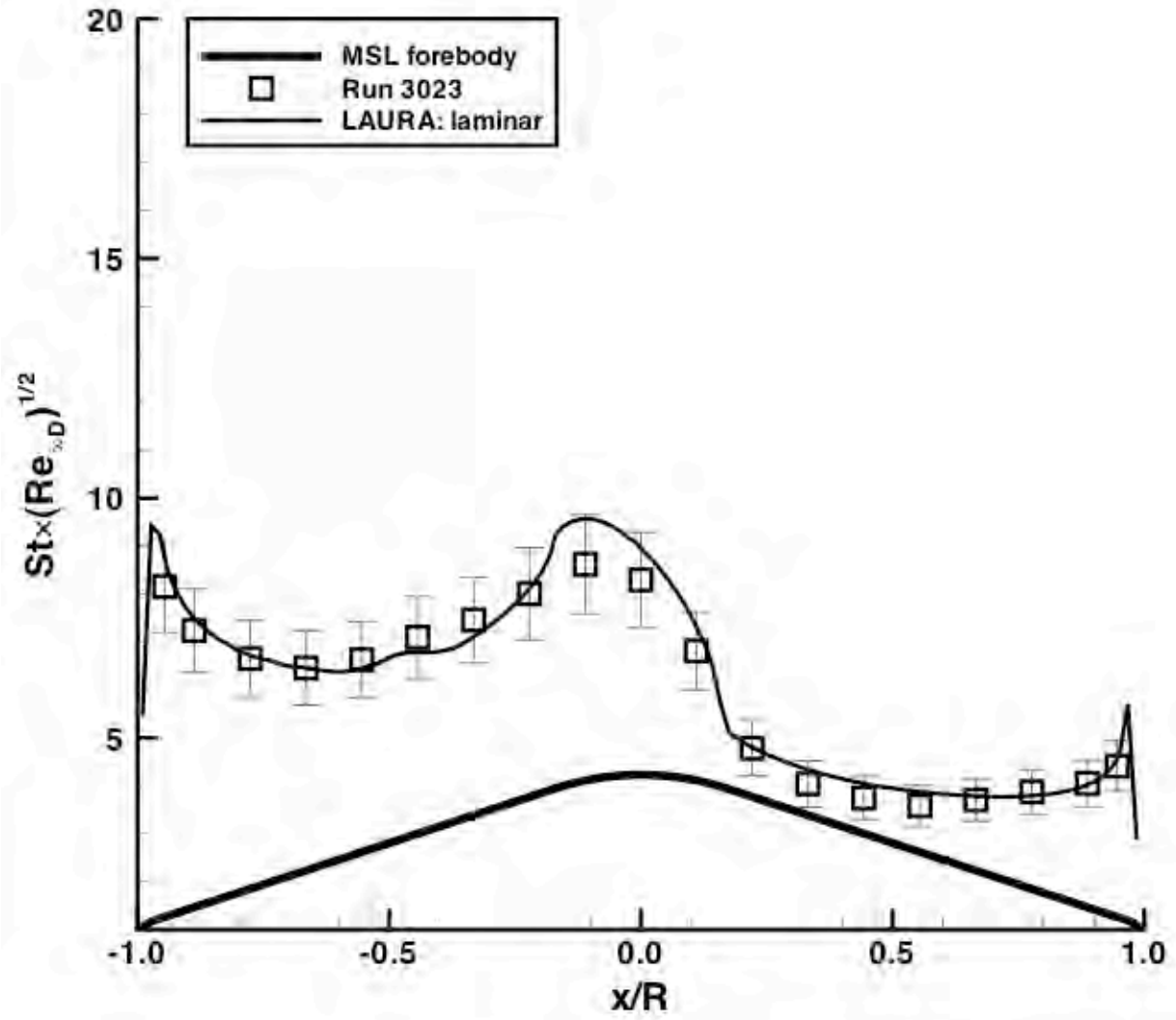


Figure 16. Comparison for Mach 10, $Re_x=8.6 \times 10^6/ft$, $\alpha=16$ deg

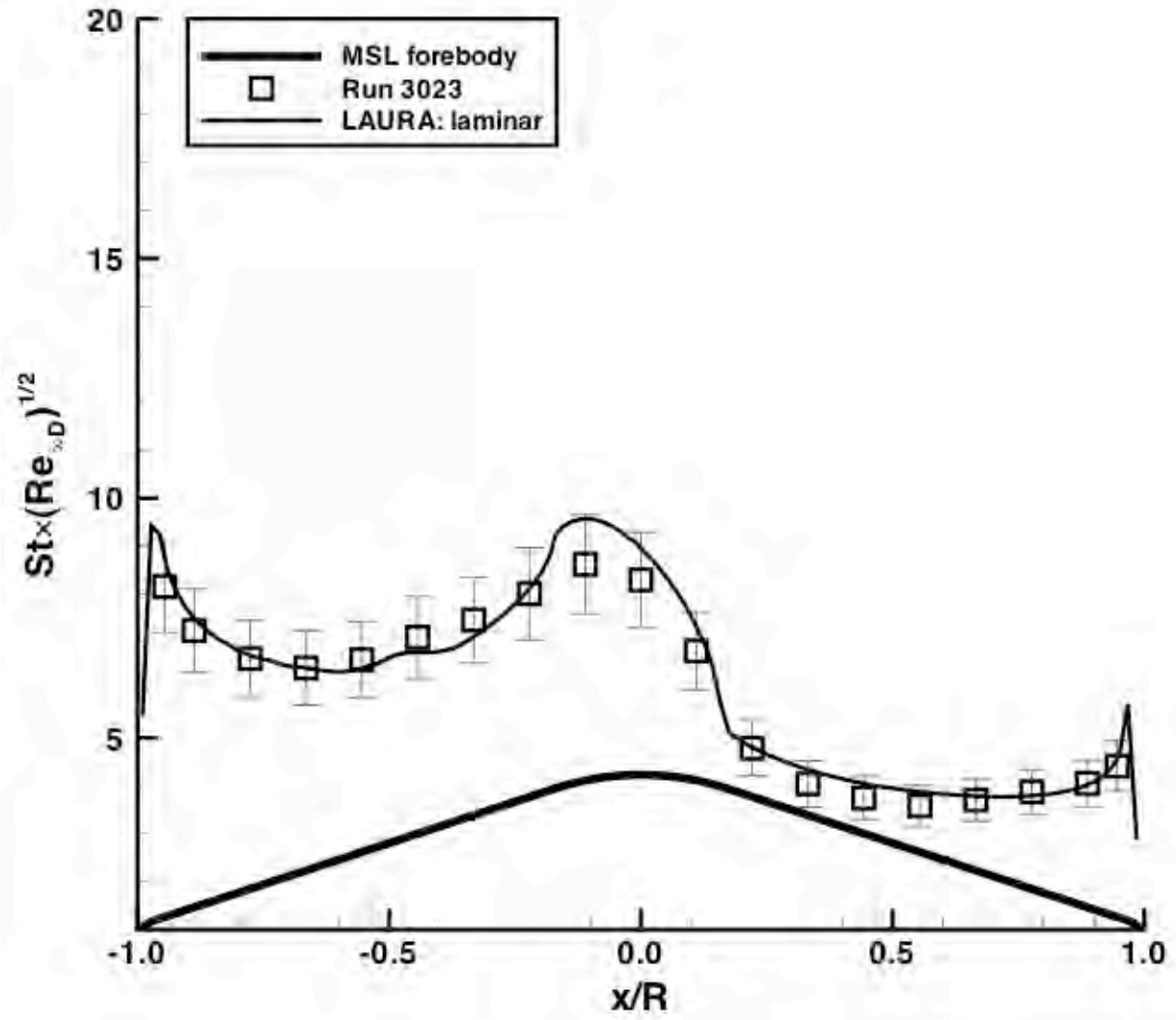


Figure 17. Comparison for Mach 10, $Re_{x,D}=14.6 \times 10^6/\text{ft}$, $\alpha=16$ deg

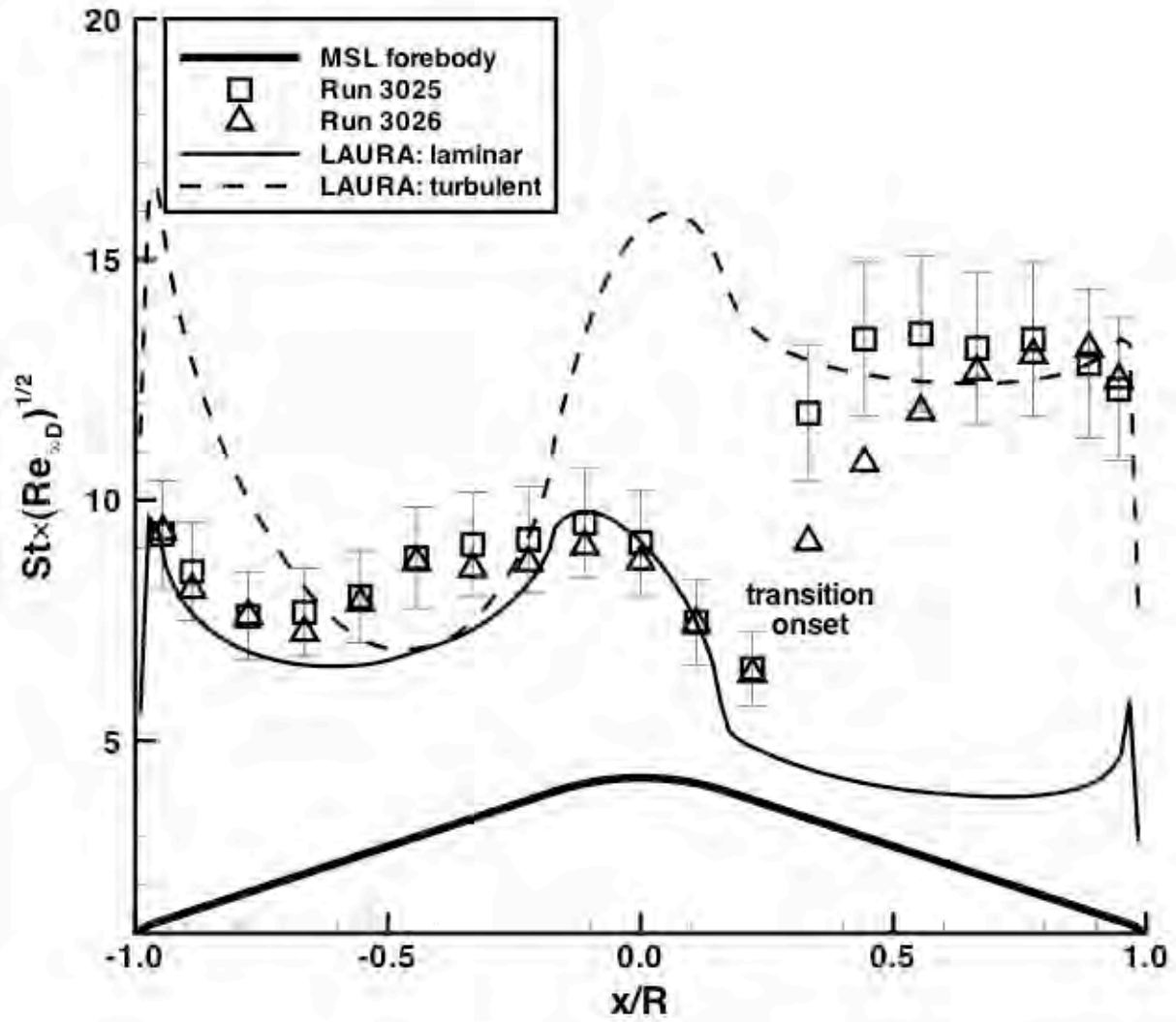


Figure 18. Comparison for Mach 10, $Re_{x,D}=18.5 \times 10^6/\text{ft}$, $\alpha=16$ deg

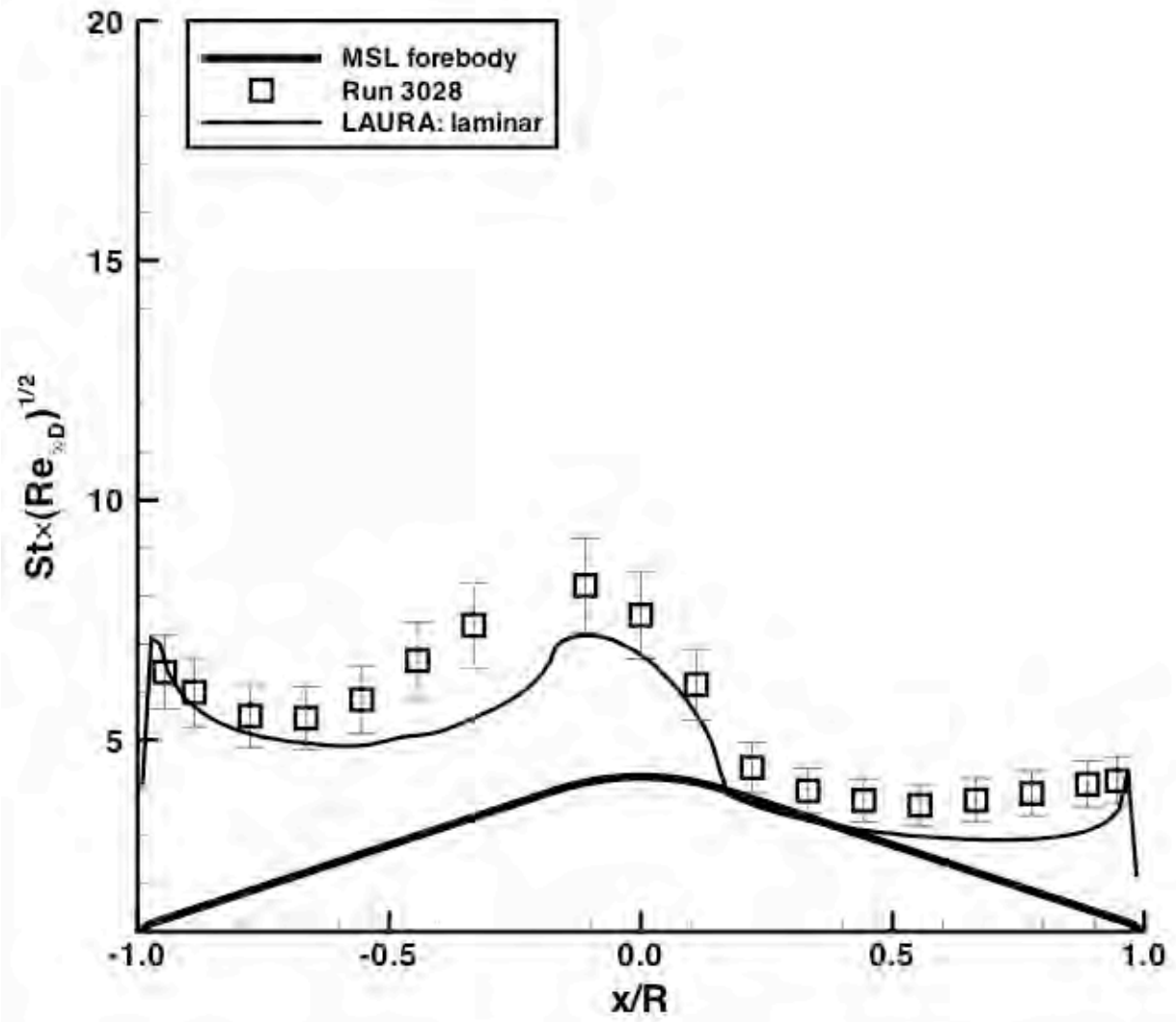


Figure 19. Comparison for Mach 8, $Re_x=4.1 \times 10^6/\text{ft}$, $\alpha=16$ deg

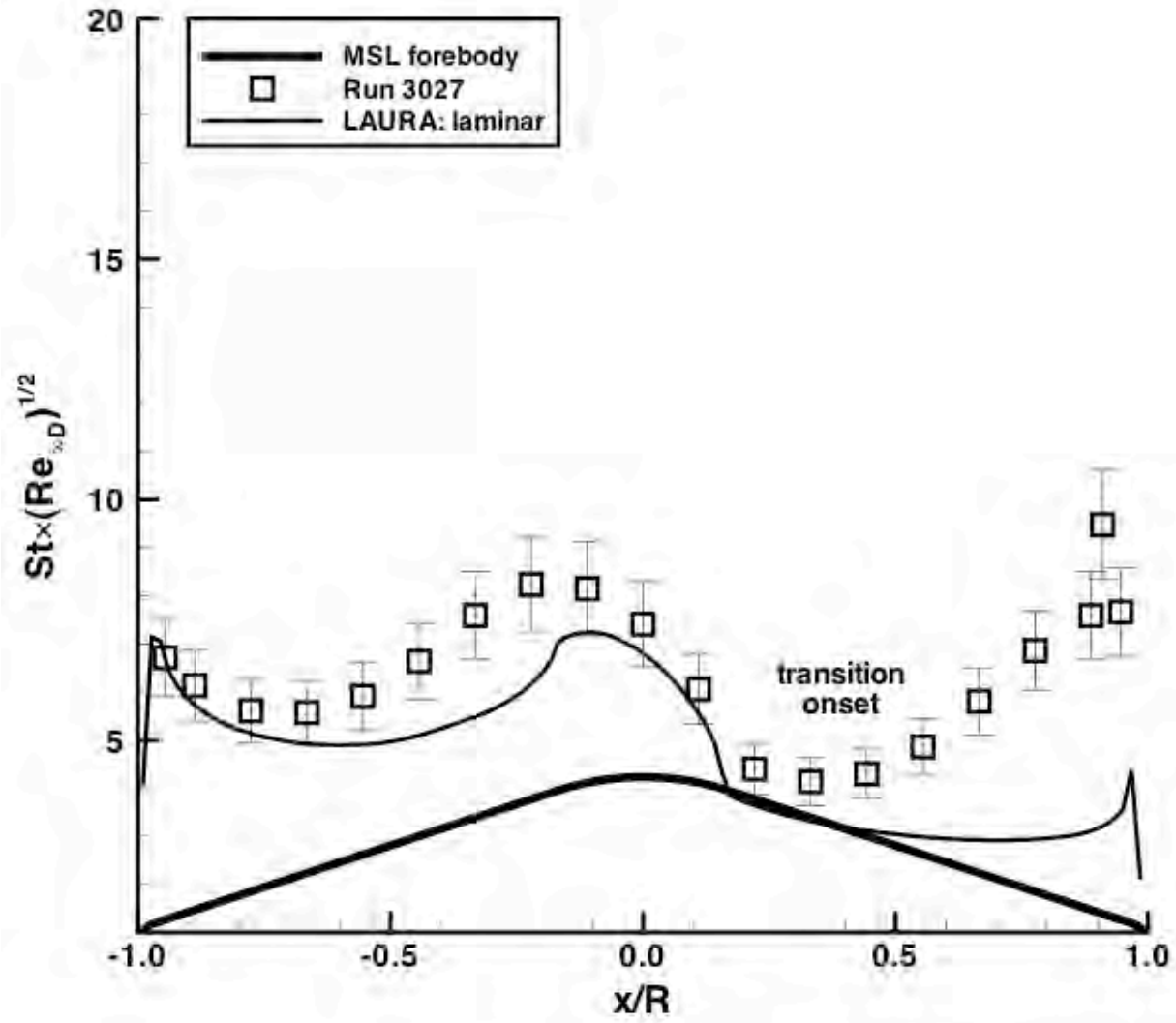


Figure 20. Comparison for Mach 8, $Re_x=8.0 \times 10^6/ft$, $\alpha=16$ deg

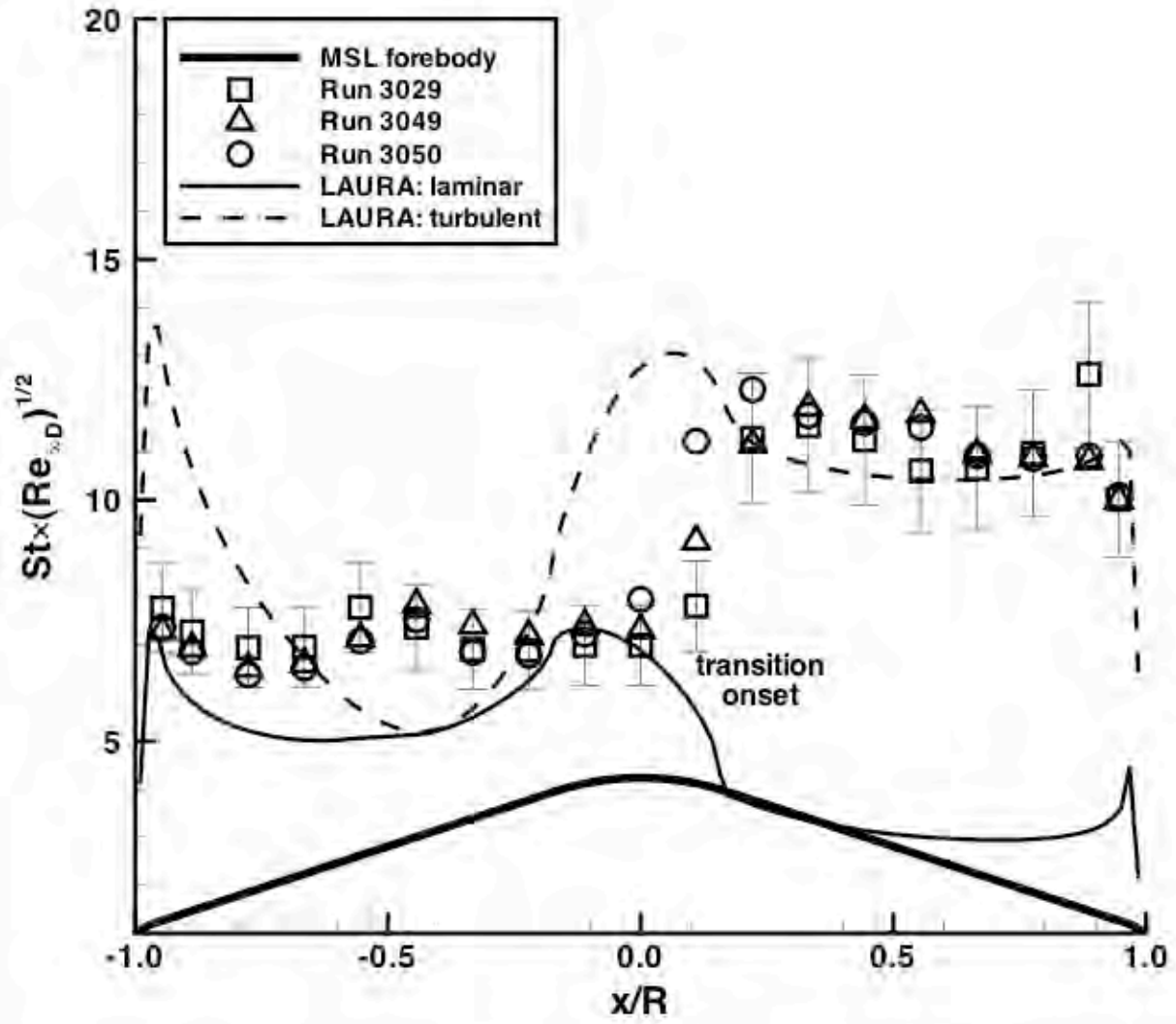


Figure 21. Comparison for Mach 8, $Re_{\infty}=16.1 \times 10^6/ft$, $\alpha=16$ deg

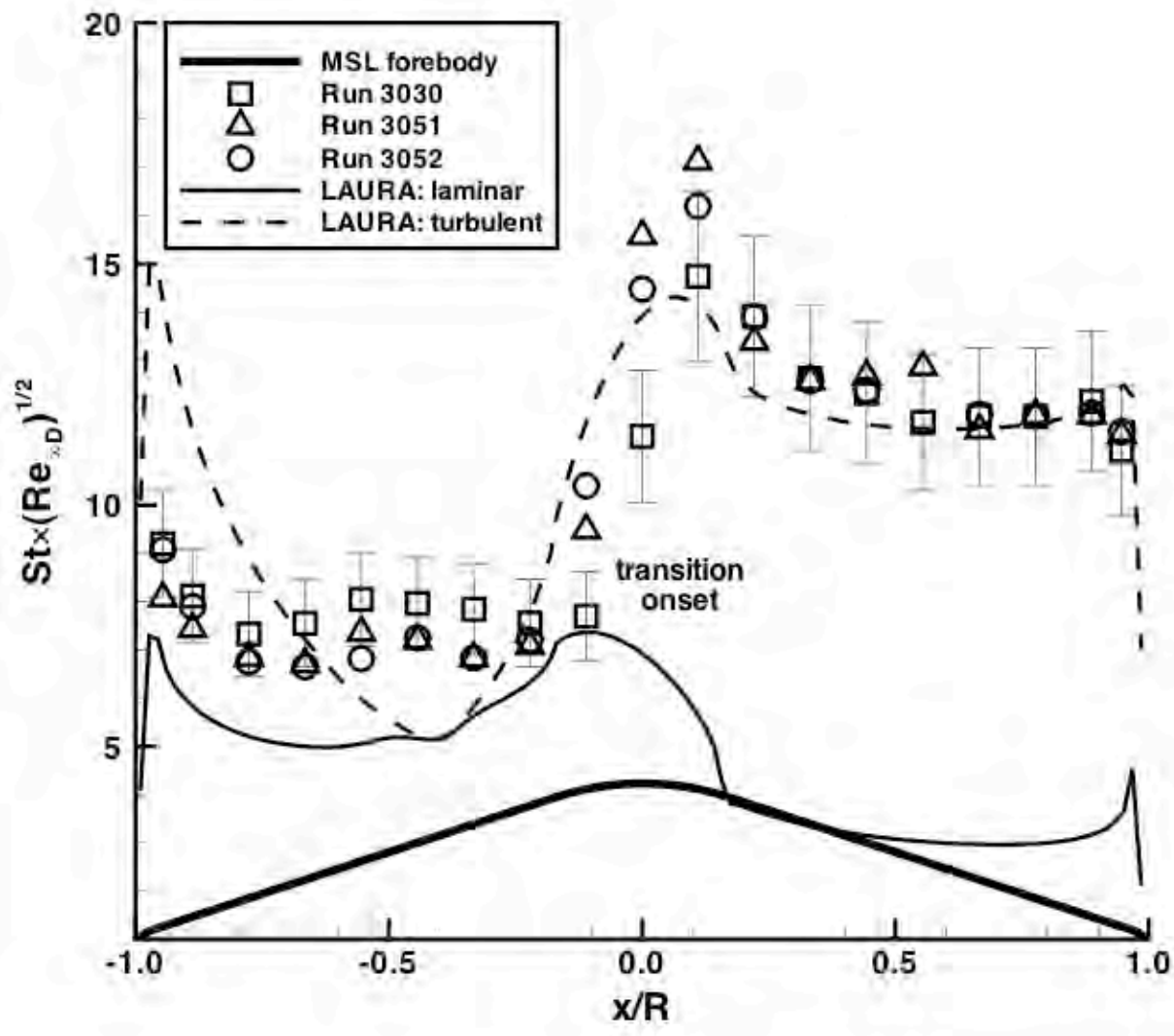


Figure 22. Comparison for Mach 8, $Re_{\infty}=21.8 \times 10^6/ft$, $\alpha=16$ deg

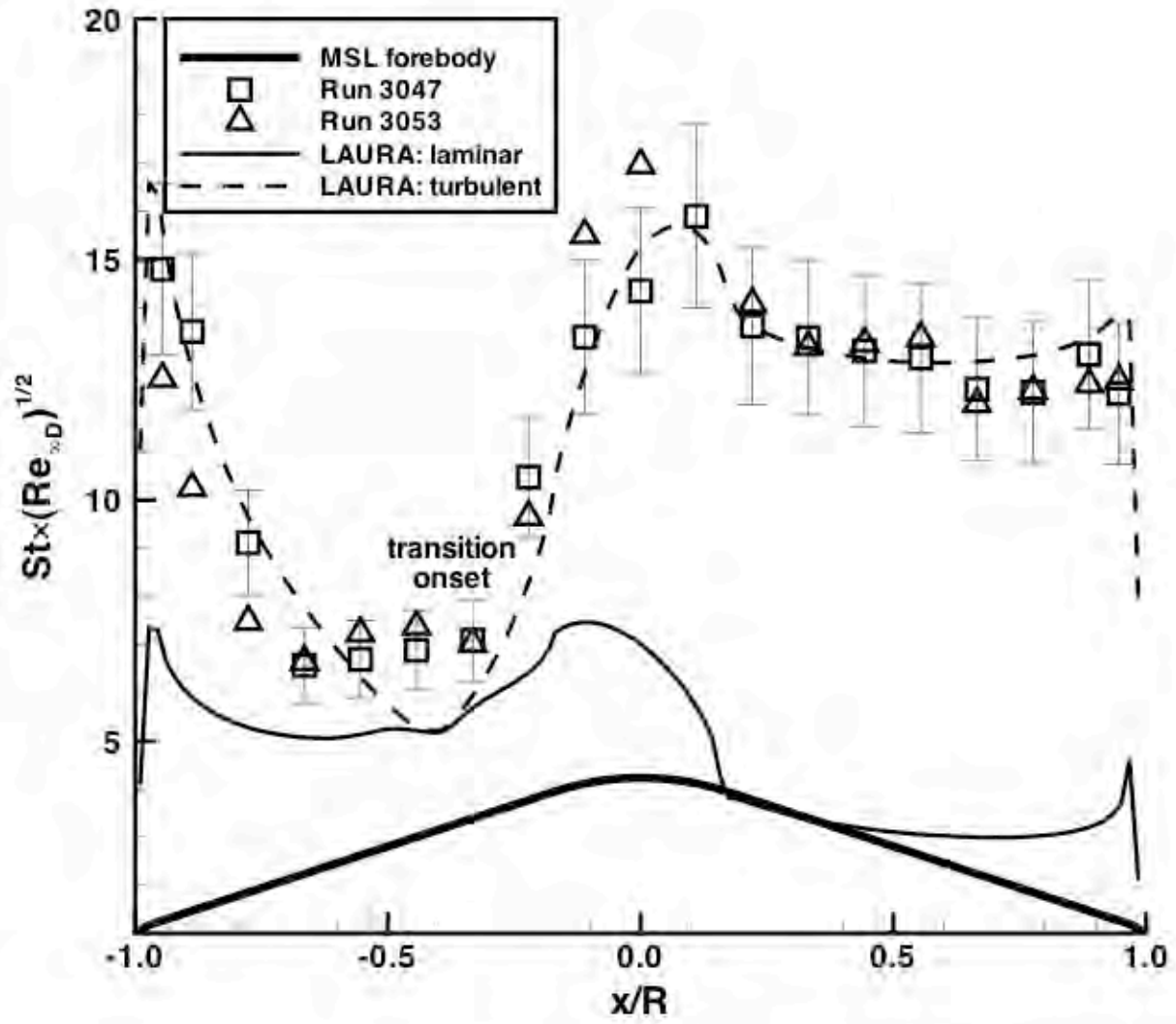


Figure 23. Comparison for Mach 8, $Re_\infty=30.6 \times 10^6/\text{ft}$, $\alpha=16$ deg

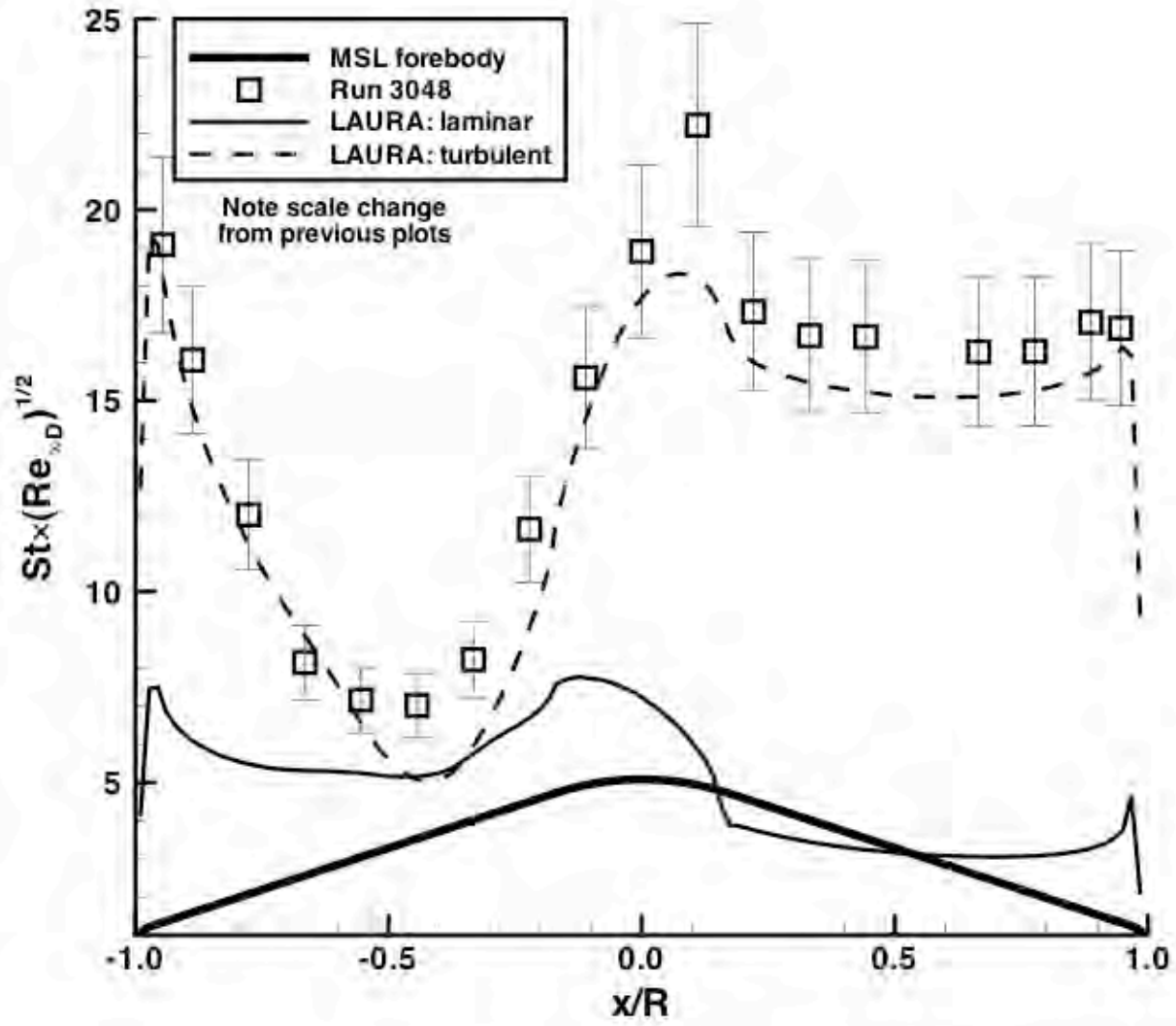


Figure 24. Comparison for Mach 8, $Re_\infty=49.6 \times 10^6/\text{ft}$, $\alpha=16$ deg

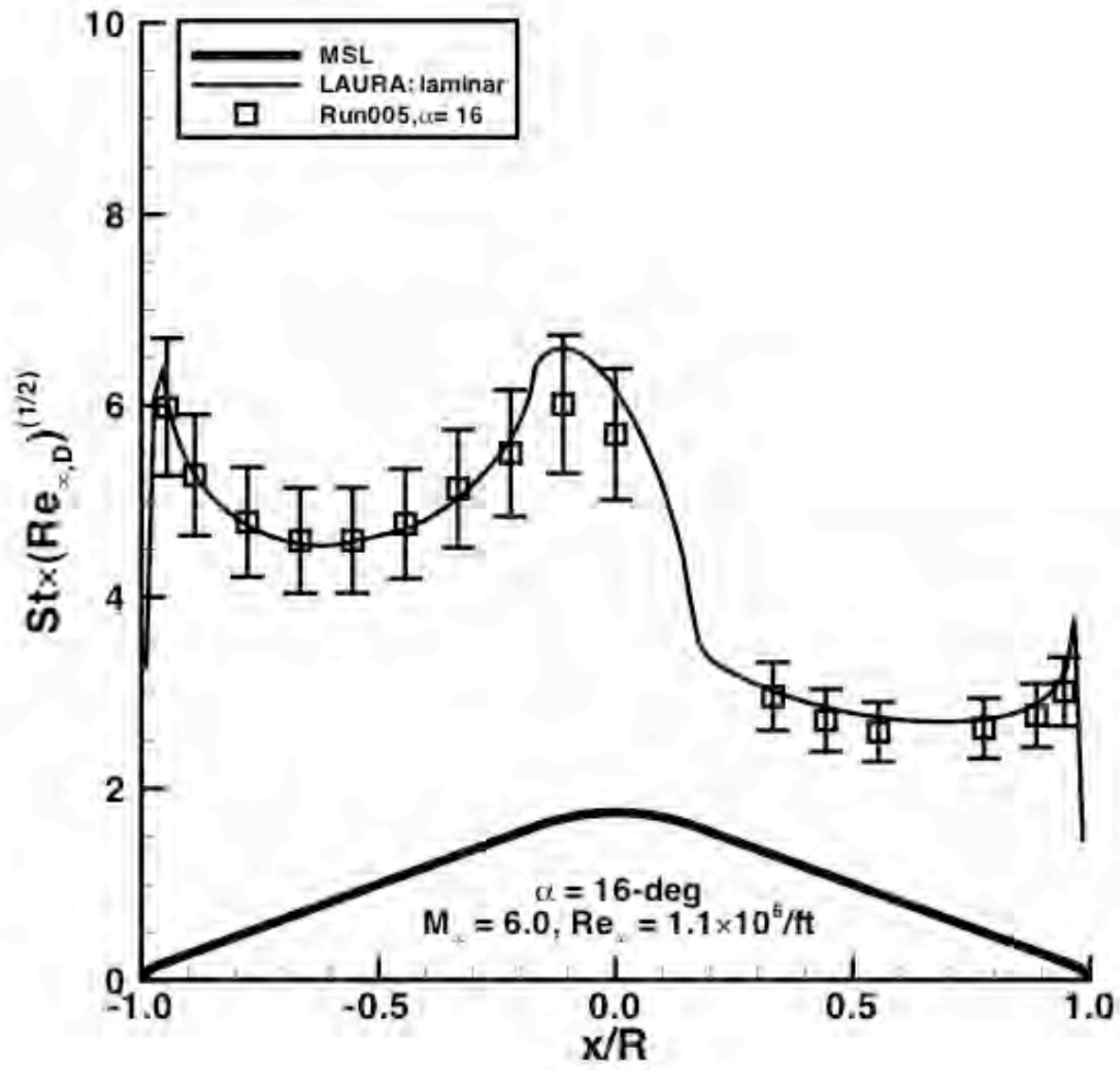


Figure 25. Comparison for Mach 6, $Re_\infty = 1.1 \times 10^6/\text{ft}$, $\alpha = 16$ deg (LaRC 20-Inch Mach 6 Air)

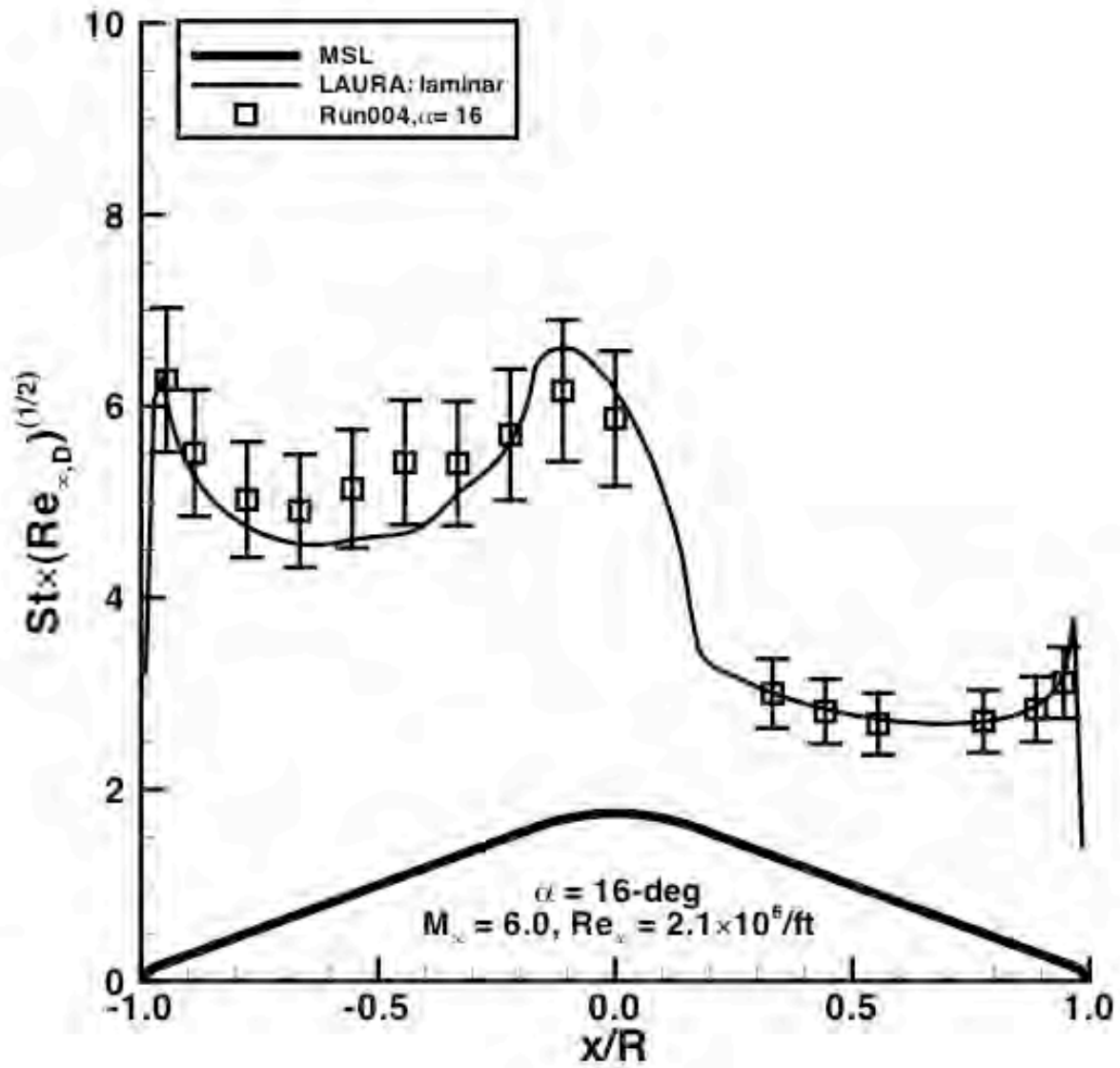


Figure 26. Comparison for Mach 6, $Re_\infty = 2.1 \times 10^6/\text{ft}$, $\alpha = 16$ deg (LaRC 20-Inch Mach 6 Air)

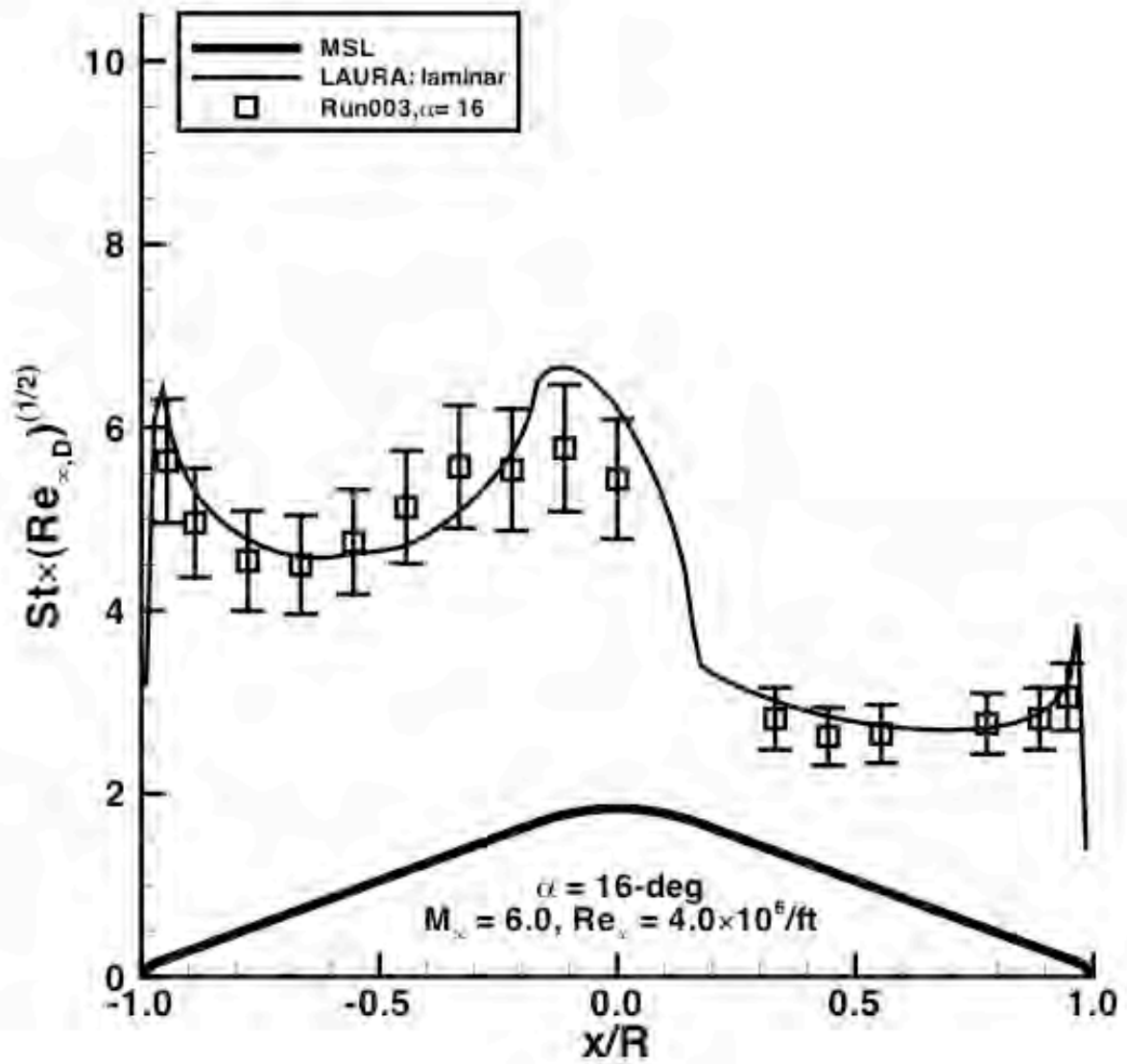


Figure 27. Comparison for Mach 6, $Re_\infty=4.0 \times 10^6/\text{ft}$, $\alpha=16$ deg (LaRC 20-Inch Mach 6 Air)

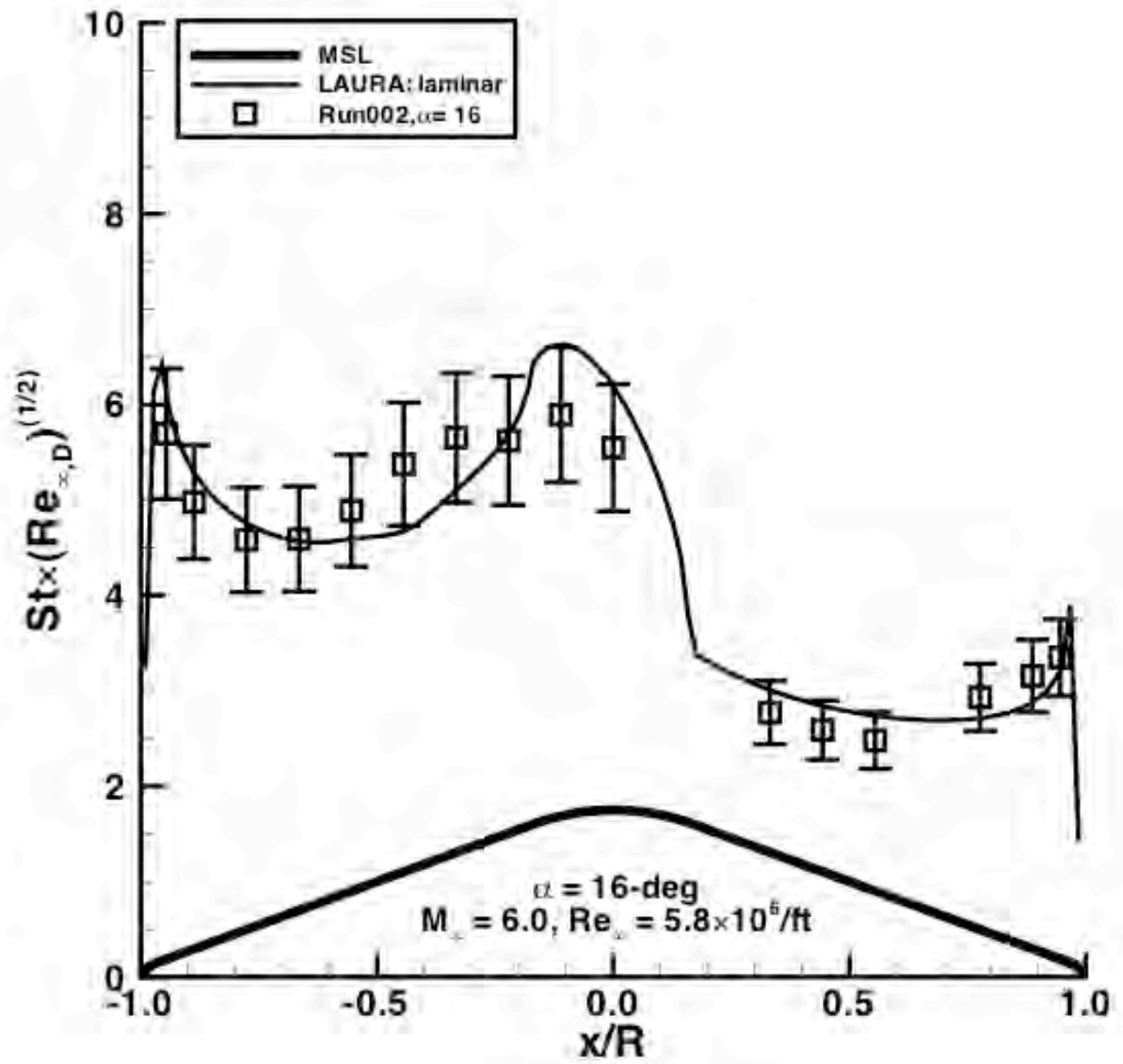


Figure 28. Comparison for Mach 6, $Re_\infty=5.9 \times 10^6/\text{ft}$, $\alpha=16$ deg (LaRC 20-Inch Mach 6 Air)

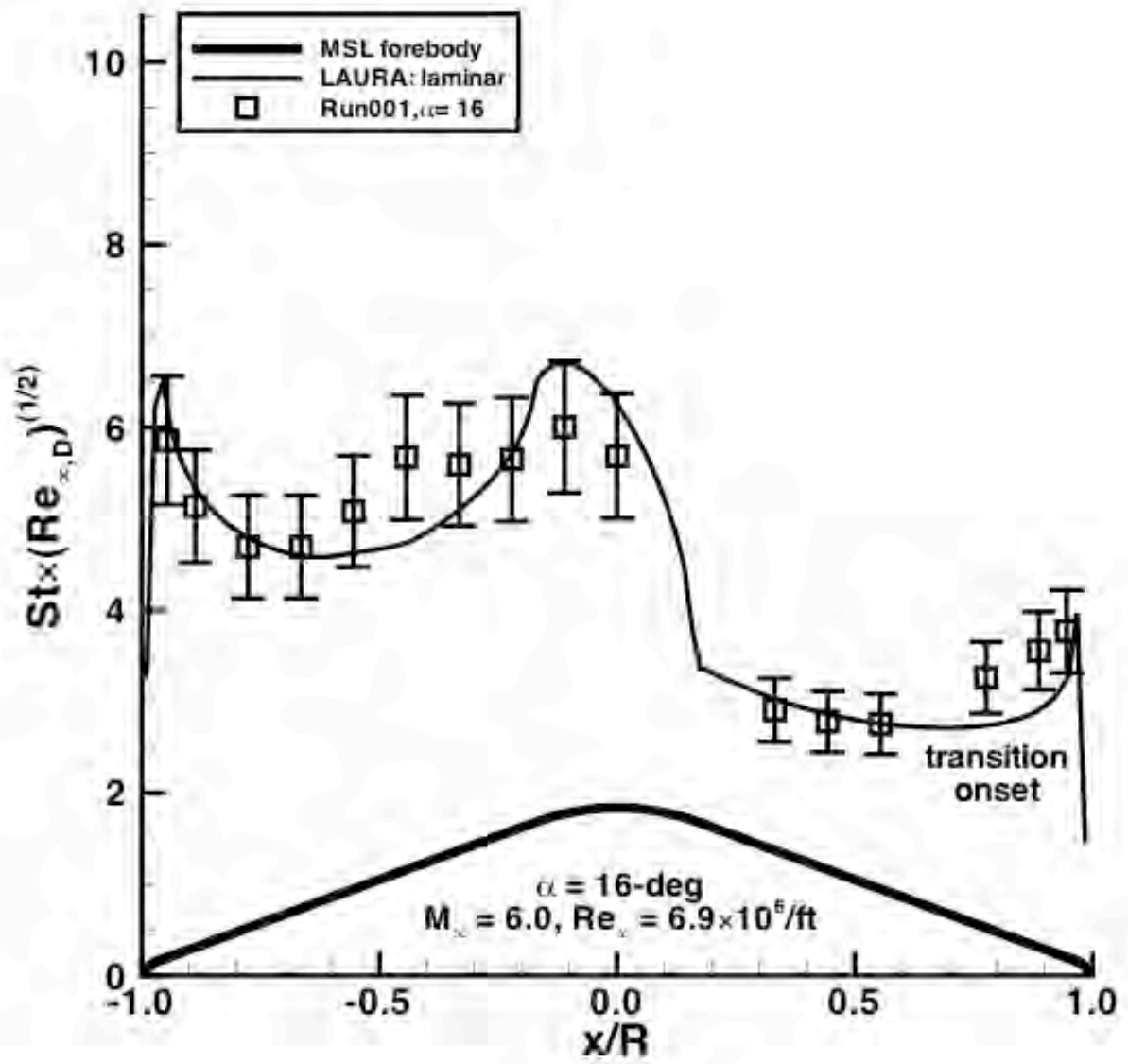


Figure 29. Comparison for Mach 6, $Re_\infty = 6.9 \times 10^6/\text{ft}$, $\alpha = 16$ deg (LaRC 20-Inch Mach 6 Air)

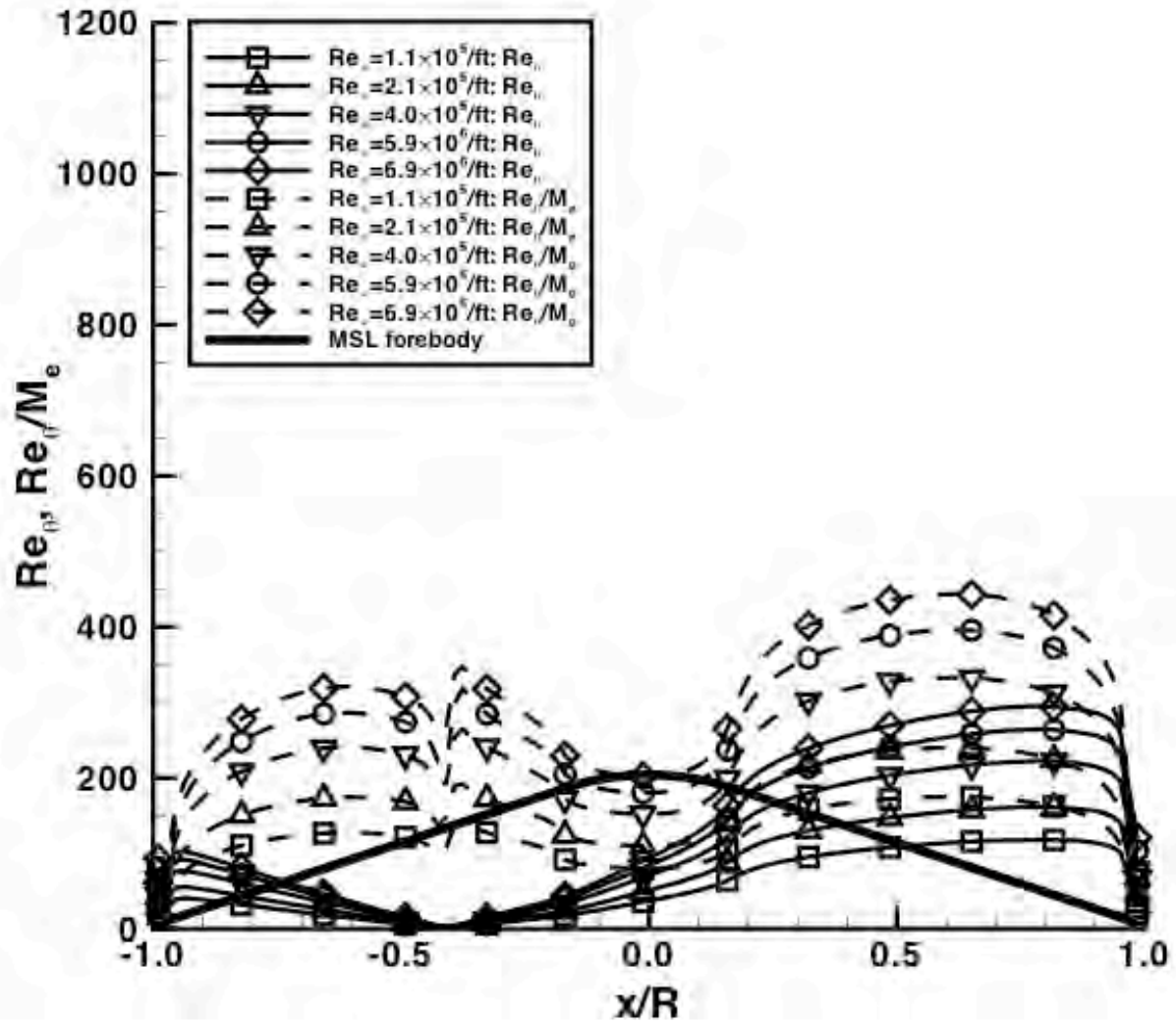


Figure 30. Boundary-layer parameters for LaRC 20-Inch Mach 6 Air Tunnel conditions